Modeling of synchrotron-based laboratory simulations of Titan's ionospheric photochemistry

Zhe Peng, Nathalie Carrasco, Pascal Pernot

GeoResJ 1–2 (2014) 33–53

Contents lists available at ScienceDirect

GeoResJ

journal homepage: www.elsevier.com/locate/GRJ

Modeling of synchrotron-based laboratory simulations of Titan's ionospheric photochemistry

Z. Peng [a], N. Carrasco [b,c], P. Pernot [a,*]

[a] Laboratoire de Chimie Physique, UMR8000, CNRS, Univ Paris-Sud, F-91405 Orsay, France
[b] Université de Versailles Saint-Quentin, CNRS/INSU, LATMOS, UMR 8190, F-78280 Guyancourt, France
[c] Institut Universitaire de France, 103 Bvd St-Michel, 75005 Paris, France

ARTICLE INFO

Article history:
Received 28 October 2013
Revised 10 February 2014
Accepted 27 March 2014
Available online 8 May 2014

Keywords:
Titan
Photochemistry
Modeling
Uncertainty analysis
Laboratory simulation
N_2/CH_4 plasma

ABSTRACT

The APSIS reactor has been designed to simulate in the laboratory with a VUV synchrotron irradiation the photochemistry occurring in planetary upper atmospheres. A N_2—CH_4 Titan-like gas mixture has been studied, whose photochemistry in Titan's ionospheric irradiation conditions leads to a coupled chemical network involving both radicals and ions. In the present work, an ion–neutral coupled model is developed to interpret the experimental data, taking into account the uncertainties on the kinetic parameters by Monte Carlo sampling. The model predicts species concentrations in agreement with mass spectrometry measurements of the methane consumption and product blocks intensities. Ion chemistry and in particular dissociative recombination are found to be very important through sensitivity analysis. The model is also applied to complementary environmental conditions, corresponding to Titan's ionospheric average conditions and to another existing synchrotron setup. An innovative study of the correlations between species concentrations identifies two main competitive families, leading respectively to saturated and unsaturated species. We find that the unsaturated growth family, driven by C_2H_2, is dominant in Titan's upper atmosphere, as observed by the Cassini INMS. But the saturated species are substantially more intense in the measurements of the two synchrotron experimental setups, and likely originate from catalysis by metallic walls of the reactors.

1. Introduction

Titan's ionosphere extends above 800 km of altitude, with local pressures no higher than 10^{-5}–10^{-6} mbar. In such diluted conditions, the efficient organic chemistry detected by mass spectrometers onboard the Cassini orbiter was unexpected, and revived our understanding of the organic chemistry occurring in Titan's atmosphere [1–18]. Large condensable molecules responsible for the nucleation leading to solid atmospheric aerosols are now known to be produced in the ionosphere [9,19–22]. The reason for the chemical growth in spite of the low molecular density has been found in the chemical coupling between radicals and reactive charged species present in the ionosphere, *i.e.* positive ions, negative ions and electrons [22].

The complexity of the chemistry is however far from being charted, as illustrated by the absence of data on the dissociative recombination products for species larger than four carbon and/or nitrogen atoms [23–25], or even for modest size ions of importance in Titan's ionosphere, such as $CH_2NH_2^+$ [17]. The initial steps of molecular growth following EUV photolysis of $N_2/CH_4/C_2H_2$ mixtures were studied, at the second time-scale, in an ion trap by Thissen et al. [26]. No substantial growth was observed in these conditions, unless C_2H_2 was present in the initial mixture. On the other hand, at the much longer time-scale of Titan's ionosphere, a correlation analysis of the positive ions densities recorded by Cassini's Ion and Neutral Mass Spectrometer (INMS) enabled Westlake et al. [18] to infer small growth units having one or two carbon atoms.

To complete and more easily approach in the laboratory this partially ionized chemistry starting with N_2/CH_4, a new generation of photochemical reactors has been developed [27,28]. In this case, VUV synchrotron sources are used to simulate the VUV part of the solar spectrum, the major source of ionization in Titan's ionosphere. A first series of results was obtained with the "Atmospheric Photochemistry Simulated by Synchrotron" (APSIS) experiment using a mass spectrometer for neutrals detection, and compared with Cassini's data [28]. The trends on the neutral species are in

* Corresponding author. Tel.: +33 1 69 15 54 28.
E-mail address: pascal.pernot@u-psud.fr (P. Pernot).

http://dx.doi.org/10.1016/j.grj.2014.03.002
2214-2428/

agreement with Titan's observations: an efficient organic growth and the formation of nitrogen-bearing products.

However no analytical device enabled the direct detection of the ions in the reactive medium. Knowing their central role in the organic growth in Titan's atmosphere, our aim is to design a fully coupled model to theoretically probe the ion content in the APSIS reactor and interpret the results observed on the neutral species. Building an exhaustive chemical model involving all the known and partially known processes, as well as their uncertainties to perform uncertainty propagation and sensitivity analysis, prevents from a complex description of the dynamics within the APSIS reactor.

As a first approach, the study is performed with a 1-cell model, run in reference conditions corresponding to the experiments reported in Peng et al. [28]. These results are used to validate the model and perform uncertainty and sensitivity analysis to highlight prominent processes explaining the observed chemical growth. Complementary model runs have been performed for different conditions of the physical parameters (irradiation spectrum, pressure, temperature) and compared to the reference one to infer the impact of these parameters in laboratory simulations and different environments. Finally, the model has been run in conditions similar to the experiments of Imanaka & Smith [27] for comparison with APSIS, and in Titan-like conditions.

The model is established in Section 2, describing the main characteristics of the APSIS reactor, the chemical scheme, the chemistry-transport 1-cell model, and the generation of electron-impact mass spectra. The probabilistic description of the uncertain chemical parameters, and notably new wavelength-dependent photolysis branching ratios, and the method to handle it are also developed in this section. Application of the model to the APSIS reactor is presented in Section 3.1. The stationary state mole fractions of the products are analyzed and compared to experimental data. Exploration of the Monte Carlo samples generated for uncertainty analysis is performed with several objectives: (i) identification of the main uncertainty sources, in terms of reaction type and specific reactions (key reactions); (ii) detection of species communities in the chemical network to identify dominant growth pathways. This section is completed with the analysis of simulations in different physical conditions (irradiation spectrum, pressure and temperature). The following sections are devoted to the analysis of simulations of Imanaka & Smith's reactor (Section 3.2), and to a proxy of Titan's ionospheric conditions (Section 3.3). The conclusion outlines the main results of this research in relation with the detailed chemical modeling of N_2/CH_4 plasmas and the representativity of laboratory simulations of Titan's ionospheric chemistry.

2. The N_2/CH_4 photochemical plasma model

2.1. The APSIS reactor

The APSIS reactor is described in detail in Peng et al. [28]. It is a stainless-steel parallelepiped with internal dimensions (length × width ce:hsp sp="0.25"/>× height) of 500 mm × 114 mm × 92 mm. The experimental conditions chosen for the modeling are reported in Table 1. A reactive gas mixture N_2/CH_4 = 90/10 (purity > 99.999%, Air Liquide) is flowed into the reactor at a gas flow of 7 standard cubic centimeter per minute (sccm), controlled by a MKS mass flow controller. A primary pumping unit ensures a stationary flow of reactive gas whose partial pressure reaches 4.5 mbar and a residence time of the gas mixture of about 180 s.

The APSIS chamber is coupled *windowless* to the DISCO beamline at SOLEIL synchrotron facility [29], using a differential pumping system [30]. A non-reactive carrier gas (He) is continuously injected between the beamline and the APSIS chamber in order to prevent the reactive mixture to be diffusing out of the reactor into the differential pumping system and leading to a total pressure of 7.0 ± 0.1 mbar in the reactor. The experiments are conducted at room temperature.

In situ measurement of the gas phase composition is achieved using a Pfeiffer QME 200 quadrupole mass spectrometer (MS). The MS detector has a resolution of 1 u and covers the 1–100 u range. Electron energy is 70 eV. Gas is sampled by a capillary tube mobile along the reactor length and probing at about 1 cm from the irradiated column. This tube is long enough to reduce the conductance between the reactor chamber and the MS, with the consequence that only stable molecules can be detected with this setup.

The photon flux of the DISCO beamline (a few 10^{11} ph s^{-1} for 0.1 nm bandwidth) leads to a N_2 dissociation ratio of less than 10^{-4}. The signal at m/z 28 of N_2 is therefore constant enough throughout the experiments to be considered as a fixed reference, and it is used to normalize the mass spectra (Section 2.4).

2.2. The reaction scheme

The present chemical scheme incorporates the complete neutral chemistry, *i.e.* photodissociation, bimolecular thermal reactions and trimolecular thermal recombinations, from Hébrard et al. [31,32], with new developments for the photodissociation branching ratios of $CH_4, N_2, H_2, C_2H_2, C_2H_4, C_2H_6$ and HCN, following Gans et al. [33], as described in Section 2.2.1. In addition, the model implements the ion chemistry database established by Carrasco et al. [34] and Plessis et al. [23], including photo-ionizations, ion–molecule reactions and dissociative recombinations involving C, H and N. Oxygen chemistry is excluded, since O_2 is just a trace gas in the reactor and, according to GC–MS analysis, does not play a significant role in APSIS photochemistry [28]. The single electron source in the APSIS reactor being photoelectrons, with insufficient energy to ionize the medium, electron impact reactions are not included.

The present chemical scheme considers only positive, singly charged ions. The DISCO spectrum intensity is vanishing below 50 nm, which prevents the double ionization of N_2 [35] and CH_4 [36], and therefore a sizeable production of dications. Negative ions have been identified as interesting vectors for the formation of heavy particles in Titan's ionosphere [14] and chemical plasmas [37], but their formation by attachment of thermal electrons involves essentially minor radical species and proceeds at very small rates [14].

In total, the model includes 244 species (125 neutrals and 119 ions) reacting with each other through 1708 reactions (33 photolysis, 415 bimolecular reactions, 82 termolecular reactions, 574 dissociative recombinations, 604 ion–molecule reactions). All the parameters describing the rate constants of these processes are uncertain (some of them unknown). They are represented by random variables with prescribed distributions, following Hébrard et al. [31,32], Carrasco et al. [34] and Plessis et al. [23].

The present model is original for two reasons: (1) it implements a new consistent treatment of the separation between photolysis cross-section and branching ratios, which are typically measured in different experiments (see next section); and (2) it is the single ion–neutral coupled model implementing the state-of-the-art dissociative recombination scheme developed by Plessis et al. [23], which for the first time includes all available data for this process, notably the partial measurements of branching ratios.

2.2.1. Representation of photolysis cross-sections and branching ratios

In previous works, photolysis rate constants were treated as lognormally distributed uncertain parameters [38,32,31,39]. In Peng et al. [40] and Gans et al. [33], the separation of photolysis cross-sections and branching ratios was proposed for several

Table 1
Summary of the conditions for the simulations in this study. I_0: integrated photon flux (from 50 to 200 nm); L: reactors length, A: reactor cross-section (width x height); P: total pressure; T: temperature; τ_r: residence time; $N_2 : CH_4$: composition of reactant gas; ρ_{CH_4}: methane relative consumption at stationary state.

Scenario	Spectrum	I_0 (ph m^{-2} s^{-1})	L (m)	A(cm^2)	P (Pa)	T (K)	τ_r (s)	N_2:CH_4	ρ_{CH_4}(%)
APSIS	DISCO	2×10^{12}	0.5	105	700	300	284	90:10	0.07
60 nm	60 nm	–	–	–	–	–	–	–	5.0
82 nm	82 nm	–	–	–	–	–	–	–	3.3
Sun	Solar	–	–	–	–	–	–	–	0.008
Low P_{re}	DISCO	–	5×10^5	–	7×10^{-4}	–	–	–	0.07
Low T	DISCO	–	–	–	–	150	–	–	0.03
"I & S"[a]	60 nm	8×10^{13}	0.7	120	13	300	53	95:5	70.0
"Titan"	Solar	1×10^9	5×10^5	105	7×10^{-4}	150	2.8×10^6	90:10	2.2

[a] Ref.: Imanaka and Smith [27].

reasons, the main one being that these data are typically measured separately, and that each has a specific type of measurement uncertainty, with an essential sum-to-one constraint for the branching ratios [41]. This separation has already been systematically implemented by our team for the ion–neutral reactions [34,41,42], the dissociative recombination reactions [23], and recently for the neutral pathways of CH_4 photolysis [33]. This line was pursued here for the main photolysis processes, and their neutral and ionic products. Moreover, the elaboration of informed wavelength-dependent representations for branching ratios is all the more important, considering the flat spectrum of the DISCO beamline, in contrast with the Ly-α-dominated solar spectrum in the wavelength range of interest [33].

2.2.1.1. Cross-sections. For the species considered here, the uncertainty in measured cross-sections at a given wavelength is mainly due to systematic effects, such as discrepancy between different measurements or temperature effects [31,43]. By comparison, the random errors within each dataset are negligible. Considering that there is not enough information in the literature to define a wavelength-dependent uncertainty factor, we account for the dominant systematic error by adopting a representation with full inter-wavelength uncertainty correlation. On purpose, we use a wavelength-independent uncertainty factor F_{σ_i} for species i. In the Monte Carlo Uncertainty Propagation (see Section 2.3.4), random samples of the cross-sections are thus obtained through

$$\ln \sigma_i(\lambda) = \ln \sigma_i^0(\lambda) + \epsilon_i, \tag{1}$$

where we use for all wavelengths the same random number ϵ_i, sampled from a normal distribution with mean zero and standard deviation $\ln F_{\sigma_i}$. We used the uncertainty factors recommended in Hébrard et al. [31]. The reference cross-sections for N_2 and CH_4 were taken from Peng et al. [40].

2.2.1.2. Branching ratios. The rather uniform spectrum of the DISCO beamline [28], calls for a continuous representation of photolysis branching ratios. However, photolysis branching ratios are often known at sparse discrete wavelengths, and large uncertainty results from the inter-/extra-polation out of these reference points. The case of CH_4 has been treated by Gans et al. [33], who developed a novel wavelength-dependent probabilistic-tree model to account for all existing information about neutral fragmentation channels. For the photochemical model of the APSIS experiments with ionizing VUV photons, one has to complete this scheme with the ionic channels. This is true for all photolyzed species, and we extended the method proposed in Gans et al. [33].

The heterogeneity of information sources on branching ratio data is a major problem: the available data are typically composed of: (i) the nominal data and the corresponding uncertainties for the neutral channels of a large set of species in Hébrard et al. [31]; (ii) the SWRI nominal data for both neutral and ionic channels for only a few species, *i.e.* $CH_4, N_2, H_2, C_2H_2, C_2H_4, C_2H_6$ and HCN, [44]; and (iii) for CH_4, the probabilistic representation of Gans et al. [33]. There are overlaps between these data, and some contradictions as well. A set of branching ratios for ionic and neutral products, with the corresponding uncertainties, was designed as follows:

- For the species without photoionization channel in the wavelength range of the experiment, nominal data and uncertainties are taken from Hébrard et al. [32,31];
- For $N_2, H_2, C_2H_2, C_2H_4, C_2H_6$ and HCN, nominal data in the SWRI database are used, and uncertainties for neutral channels are taken from Hébrard et al. [31]. Ionic channels have no recommended uncertainty. Considering that there is generally a much higher precision for ion detection techniques than for neutrals or radicals, we use a nested scheme to preserve as much uncertainty structure as possible:

$$\mathrm{A} + \mathrm{h}\nu \longrightarrow \begin{cases} \xrightarrow{B_{neu}(1\pm\Delta B_{n/i})} \begin{cases} \xrightarrow{B_{n1}(1\pm\Delta B_{n1})} \text{Neutral Channel 1} \\ \xrightarrow{B_{n2}(1\pm\Delta B_{n2})} \text{Neutral Channel 2} \\ \ldots\ldots \end{cases} \\ \xrightarrow{B_{ion}(1\pm\Delta B_{n/i})} \begin{cases} \xrightarrow{B_{i1}(1\pm\Delta B_{i1})} \text{Ionic Channel 1} \\ \xrightarrow{B_{i2}(1\pm\Delta B_{i2})} \text{Ionic Channel 2} \\ \ldots\ldots \end{cases} \end{cases}, \tag{2}$$

where B_{neu} and B_{ion} are respectively the total neutral and ionic contributions and both have a relative uncertainty of $\Delta B_{n/i}$. $B_{n1}, B_{n2} \ldots$ and $B_{i1}, B_{i2} \ldots$ are the branching ratios of the neutral and ionic channels, respectively, and $\Delta B_{n1}, \Delta B_{n2} \ldots$ and $\Delta B_{i1}, \Delta B_{i2} \ldots$ are their corresponding relative uncertainties. For lack of data and according to their typical values in the literature [45], we assign the branching ratios of all ionic channels a 20 % relative uncertainty. Their total contribution is typically more accurate and its relative uncertainty was estimated to $\Delta B_{n/i} = 3\%$.

- The representation of the branching ratios for the photolysis of CH_4 is based on the same scheme. We apply the representation described in Gans et al. [33] to the neutral part, with a lower wavelength limit extented to 80 nm, where the neutral channels become negligible in Huebner and Link [44]. The remaining part of the representation is the same as in the previous case.

To ensure the continuity in the interpolation/extrapolation of the branching ratio data for wavelength intervals (*e.g.* branching ratios provided in SWRI [44] or recommended in Hébrard et al. [31]), we need to preserve the correlation between wavelengths in a branching ratio sample. To address the nature of these wavelength-interval data, we use the generalized Dirichlet distribution (*Dirg*), which can be easily parameterized by nominal values and

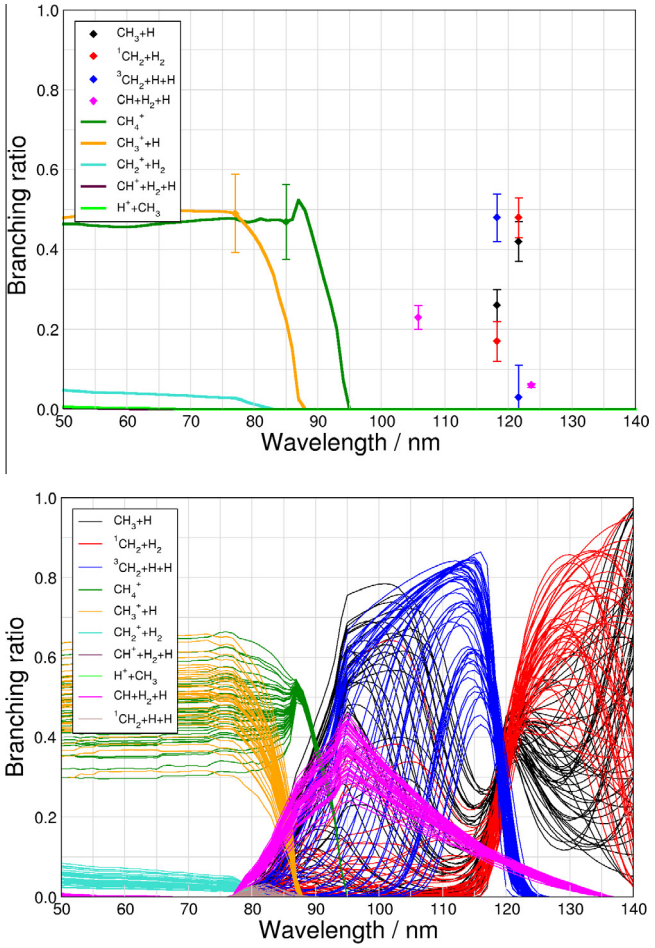

Fig. 1. Photolysis branching ratios for CH_4: (top) data and constraints used to build the probabilistic tree representation; (bottom) sample of unit-sum sets branching ratios generated from the probabilistic tree representation.

uncertainties [23]. To handle the problem of correlation in a wavelength interval during the sampling of a *Dirg* distribution, we adopt an *ad hoc* technique: while generating the values at different wavelengths in the same sample, we always retain the same random seed, hence ensuring wavelength-wise full correlation. Realizations of the random generator of photolysis branching ratios are shown in Fig. 1 for CH_4 (in this representation, one cannot see the sum-to-one constraint on the branching ratios at each wavelength).

2.3. The photochemical-transport model of the APSIS reactor

The present model has been designed to be able to represent different geometry approximations of the reactor, from 0D (1-cell model) to 2D (cylindrical symmetry). In the present study, we focus on using the full neutral-ion coupled chemical scheme, and, in order to be able to manage the parametric uncertainties, we have to consider a simplified 1-cell geometry, assuming no transport and a uniform spatial distribution of the species. However, the gas inflow and outflow are taken into account, and radiative transfer is considered through Beer–Lambert-type photoabsorption, but in the assumption of a uniform gas (Fig. 2). This section provides the details of model design and implementation.

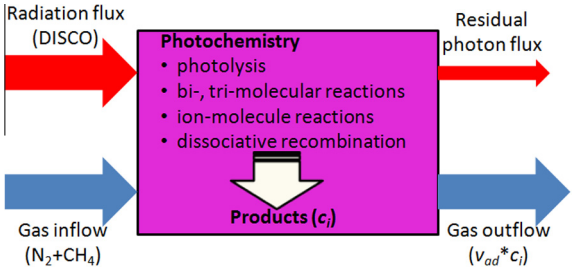

Fig. 2. Scheme of the 1-cell model.

2.3.1. Total balance and transport

It was observed that the pressure in the APSIS reactor varies very weakly during the time course of experiments and presents only a slight decrease in the direction of the gas transport [28], indicating a nearly uniform motion of the gas in the reactor. In consequence, we define a constant and uniform gas advective velocity v_{ad} (m s^{-1}) in the reactor. Assuming the ideal gas law, v_{ad} is calculated from the reactive gas inflow rate q_{re} (mol s^{-1}) and the reactive gas partial pressure P_{re} (Pa) in the reactor by

$$v_{ad} = \frac{q_{re}}{P_{re}} \frac{RT}{A}, \tag{3}$$

where A (m^2) is the reactor cross-section. The carrier gas (He) inflow rate q_{ca} is the counterpart of the reactive gas in their contribution to the total pressure P

$$q_{ca} = (P - P_{re}) v_{ad} \frac{A}{RT}. \tag{4}$$

We assume that at the exit of the reactor, the gas is pumped out also at v_{ad}, so as to ensure, in absence of reactions, the mass balance in the reactor. Hence, the residence time of the reactive gas τ_r (s) is

$$\tau_r = L / v_{ad}, \tag{5}$$

where L (m) is the reactor's length. In the presence of reactions, the concentration variations due to transport and chemistry should be considered simultaneously. Thus, the differential of concentration for the ith species, c_i (mol m^{-3}), can be written as

$$\frac{dc_i}{dt} = Q_i + R_i, \tag{6}$$

where t is the reaction time, Q_i and R_i (mol m^{-3} s^{-1}) are the concentration variations due to transport and chemistry, respectively.

Considering the single cell in the model, the term Q_i can be written as

$$Q_i = \frac{\Phi_{i,in} - \Phi_{i,out}}{L}, \tag{7}$$

where $\Phi_{i,in}$ and $\Phi_{i,out}$ (mol m^{-2} s^{-1}) are respectively the influx and the outflux of the ith species: $\Phi_{N_2,in} = f_{N_2} \times q_{re}/A, \Phi_{CH_4,in} = f_{CH_4} \times q_{re}/A, \Phi_{He,in} = q_{ca}/A$ and $\Phi_{i,in} = 0 \forall i \notin \{N_2, CH_4, He\}$, where f_{N_2} and f_{CH_4} are the proportions of the reactants in the incoming gas. For all species, one has $\Phi_{i,out} = c_i v_{ad}$.

2.3.2. Radiative transfer and photolysis rate constant

The photolysis rates depend on the actinic flux $I(x,\lambda)$ (ph m^{-2} s^{-1} nm^{-1}) at wavelength λ and distance x from the entrance of the light beam in the reactor (optical path). Considering Beer–Lambert absorption, we have

$$I(x,\lambda) = I_0(\lambda) \exp\left(-\sum_i \tau_i(x,\lambda)\right), \tag{8}$$

where $I_0(\lambda)$ describes the photon flux at the entrance, $\tau_i(x,\lambda)$ is the wavelength-dependent optical depth of the ith absorber. It depends on the species concentration $c_i(x)$ along the optical path and the photoabsorption cross-section $\sigma_i(\lambda)$ (m^2 mol^{-1}):

$$\tau_i(x,\lambda) = \sigma_i(\lambda) \int_0^x c_i(x) dx. \tag{9}$$

The photolysis rate constant of the jth channel of the ith absorber at position x, is given by

$$J_{ij}(x) = \int_{\lambda} I(x,\lambda)\sigma_i(\lambda)b_{ij}(\lambda)\mathrm{d}\lambda, \tag{10}$$

where $b_{ij}(\lambda)$ is the branching ratio at wavelength λ of this channel.

As there is a single cell in the model design of the present study, an average value of the photolysis rate constant has to be used. $J_{ij}(x)$ at the cell center, $J_{ij}(\bar{x})$, is commonly chosen in atmospheric modeling studies [38], but this is not appropriate for our model, where the rate constant can strongly vary along the optical path. Instead, we calculate the average of $J_{ij}(x)$ along the reactor length,

$$\overline{J_{ij}(x)} = \frac{1}{L}\int_0^L J_{ij}(x)\mathrm{d}x. \tag{11}$$

Based on the assumption of uniform gas density, one can easily derive

$$\overline{J_{ij}(x)} = \int_{\lambda} I_0(\lambda)\sigma_i(\lambda)b_{ij}(\lambda)\frac{1-e^{-L\sum_i(c_i\sigma_i(\lambda))}}{L\sum_i(c_i\sigma_i(\lambda))}\mathrm{d}\lambda. \tag{12}$$

To evaluate this integral, the wavelength is discretized with a resolution of 1 nm, adapted to the spectral resolution of the cross-sections database of Hébrard et al. [31]. The additional photolysis data used in this study, from the SWRI database [44], are interpolated on this wavelength grid using a Gauss–Legendre quadrature [46].

2.3.3. Integration method

The implicit-explicit Runge–Kutta–Chebyshev (IRKC) method [47], capable of integrating systems of partial differential equations (PDEs), is applied to the present model. It handles the equations by both an explicit part $F_E(t,y)$ and an implicit part $F_I(t,y)$, *i.e.*

$$y'(t) = F_E(t,y) + F_I(t,y). \tag{13}$$

For a transport-reaction model, it is suggested that F_E and F_I respectively describe the parts of a cell's differential which are respectively dependent (*e.g.* diffusion and photolysis) and independent (*e.g.* thermal reactions) on other cells. The latter, F_I, is usually regarded as a system of ordinary differential equations (ODEs) and can be very stiff, which is the case for our coupled ion–neutral model. The IRKC method is able to cope with the problem of stiffness in F_I [48].

The present model has no internal transport. In theory, the whole model could therefore be considered as a set of ODEs and solved in F_I or by other ODE solvers. However, the photolysis is treated in F_E, as in transport–reaction models, because we treat the radiative transfer explicitly, and complex evaluation of Jacobian elements for the photolysis makes it impractical to regard the photolysis rate equations as ODEs.

Besides, IRKC enables to account for diffusion: for further studies in higher dimension (1D or 2D), IRKC will be well adapted to a transport–reaction model. The part of thermal reactions, independent on other cells, could be treated implicitly and separately in each cell, so that it could be repeatedly implemented by the program. This leads to small storage requirements and good computing performance.

Tests were performed to check the convergence and stability of the stationary state of the present model integrated by the IRKC method. The stationary state is very robust to either perturbations of initial conditions or the choice of propagator tolerance parameters.

2.3.4. Uncertainty management

As the chemical parameters of the model are intrinsically uncertain, one has to evaluate the impact of this uncertainty of the input parameters on the model outputs (mole fractions of products). The formula of the propagation of distributions [49]

$$p(Y=y) = \int \mathrm{d}X_1\mathrm{d}X_2\ldots\mathrm{d}X_n p(X_1,X_2,\ldots,X_n) \times \delta(y - f(X_1,X_2,\ldots,X_n)), \tag{14}$$

provides a transformation from the joint probability density function $p(X_1,X_2,\ldots,X_n)$ of all input parameters, to that of the output(s) $Y = f(X_1,X_2,\ldots,X_n)$. From $p(Y)$, one can compute all the necessary statistics.

It is rarely possible to perform the integration above analytically. Instead, the BIPM recommends the use of Monte Carlo Uncertainty Propagation (MCUP) methods [49], in which we propagate representative samples of the inputs distributions, rather than the analytic distributions themselves. We generate random sets of input parameters according to their probability density function, and then, for each set, evaluate the corresponding outputs of the model, thus building a representative sample of the outputs distribution.

The MCUP method is convenient to treat models with many inputs and outputs. Its convergence does not depend on the number of input parameters. Moreover, it is directly applicable to multi-outputs models, through a single set of samples. As a result, the intrinsic correlation between the outputs is preserved and can be used for further analysis (Section 3.1.3).

However, the MCUP method is expensive in computer time (repeated runs of the model necessary to generate significant statistics). We limit our sampling to 500 runs, with random samples generated for each process type according to Carrasco et al. [34], Hébrard et al. [32], Plessis et al. [23] and Gans et al. [33].

2.4. Generation of mass spectra

We present here the procedure to generate electron impact mass spectra from the simulated neutral species concentrations. We adopt a 1 u mass resolution, for direct comparison with experimental spectra. The intensity, I_j, of a mass peak at *integer m/z* j is modeled by

$$I_j = \sum_i \sigma_i c_i f_{ij}, \quad j = 1,2\ldots n, \tag{15}$$

where σ_i and c_i are respectively the electron impact cross-section and the concentration of the ith species, n is the maximal mass, and f_{ij} is the fragmentation pattern of the ith species at m/z j, with the constraint $\sum_{j=1}^{n} f_{ij} = 1$ [50].

The electron impact cross-sections for a $C_xH_yN_z$ species are modeled by the formula proposed by Puccio and Miller [50]

$$\sigma_i/\text{Å}^2 = 0.460x + 1.086y + 1.348z. \tag{16}$$

The fragmentation patterns for almost all stable species up to 6 heavy (C, N) atoms and some heavier species are extracted from the NIST Chemistry Webbook [51], well covering the stable species of interest in the present study, and including Earth natural isotopic abundances. However, this database provides no fragmentation data for radicals and there are only few data of this type in the literature. In consequence, we chose to exclude the radicals from the MS. Finally, we average the fragmentation patterns of isomers, if they are not distinguished in the model. For example, C_3H_6 in our model represents both propene and cyclopropane: their fragmentation patterns are averaged with equal weights.

In details, the generation of the neutral MS from a Monte Carlo sample of species concentrations proceeds according to the following steps:

1. Perform the Monte Carlo loop by calculating the *k*th *sample* of the intensities $I_j^{(k)}, (j = 1, 2 \ldots n; k = 1, 2 \ldots m)$ at different *m/z* from the *k*th of *m samples* of the species concentrations $c_i^{(k)}$ by

$$I_j^{(k)} = \sum_i \sigma_i c_i^{(k)} f_{ij}, \quad j = 1, 2, \ldots, n; \; k = 1, 2 \ldots m. \tag{17}$$

2. Normalize, within *each set of samples*, the intensities with respect to that at *m/z* 28 (molecular ion signal of N_2, the most abundant species), for comparison with other experimental mass spectra.
3. Generate statistics of the normalized intensities.

Note that the estimated electron impact cross-sections (Eq. (16)) and the NIST fragmentation patterns [51] are uncertain. However, compared to the relative uncertainties on the kinetic parameters and the species concentrations (often larger than 100%), their relative uncertainties (∼10% [50]) are treated as negligible.

There are some sources of bias to be considered when comparing the simulated MS to experimental ones: (i) the APSIS and the NIST standard MS were measured at different pressures, which may significantly influence the fragmentation patterns [28]; (ii) different mass spectrometers may overlap the major peaks (*e.g.* *m/z* 28) with neighboring peaks in different ways, interfering in the determination of the intensities of these minor peaks. These effects are difficult to quantify, and are not accounted for in the generation of the simulated MS.

3. Results and discussion

The 1-cell model has been run in reference conditions corresponding to the APSIS experiments [28]. These results are used to evaluate the model and perform uncertainty and sensitivity analysis. Additional sets of model runs have been performed for different conditions of the physical parameters (irradiation spectrum, pressure, temperature) and compared to the reference one to infer the impact of these parameters in laboratory simulations. Finally, the model has been applied to conditions similar to the experiments of Imanaka & Smith [27] , and to a rough proxy of Titan's ionosphere. The parameters for all simulations are reported in Table 1.

3.1. Simulation of the APSIS reactor

The reference case of the APSIS model corresponds to the experiments at 7 sccm, which were available when we began to develop the model [28]. The physical conditions of the reference case are: $P = 7$ mbar (700 Pa), $T \simeq 300$ K and a reactive gas inflow $q_{re} = 7$ sccm (4.7×10^{-6} mol s^{-1}), resulting in a gas residence time of 284 s (Table 1).

We integrate this model until the system reaches a stationary state (SS), *i.e.* about 1000 s after the start of irradiation. This time is comparable to the largest time constant measured in the APSIS experiments, for the peak at *m/z* 52 (990 s) [28].

3.1.1. Comparison to experimental results

The distribution of the stationary state mole fractions (normalized to N_2) is presented in Fig. 3. Starting from the C2 block, the concentrations of stable neutrals globally decrease with their mass. The main C2 species, *i.e.* C_2H_2, C_2H_4, C_2H_6 and HCN, have mole fractions around 10^{-5}, and the main C3 (C_3H_6, C_3H_8, *etc.*), C4 (C_2H_3CN, C_4H_8, *etc.*) around 10^{-6} and 10^{-7}, respectively. In the C7 and C8 blocks, several species still have a mole fraction between 10^{-10} and 10^{-15},*e.g.* C_7H_4, C_7H_6 and C_8H_2.

The total mole fraction of ions is about 10^{-9}. The decrease of ion concentrations with mass is less evident than for neutrals. Most of the major ions (from C1 to C10) have mole fraction between 10^{-10} and 10^{-15}.

The stationary state CH_4 consumption ratio

$$\delta_{CH_4} = \frac{[CH_4]_0 - [CH_4]_{SS}}{[CH_4]_0}, \tag{18}$$

in the experiments and in the model are respectively $\delta_{CH_4} = 0.30 \pm 0.06\%$ and $0.07 \pm 0.01\%$. They are not in perfect agreement, but, considering the model simplicity and absence of adjustable parameters, a factor of 4 is tolerable. More specifically, the simplified description of advection and radiative transfer in the 1-cell model may result in a bias of the effective gas residence time and in consequence of the methane consumption.

Some species predicted by the present model were not identified in the APSIS *in situ* mass spectra, *e.g.* NH_3 and CH_2NH, because their parent MS peaks are hidden by the signals of OH^+ and $^{14}N^{15}N^+$. But their formation is confirmed in the PAMPRE reactor in similar conditions [52], and thus likely also in the APSIS experiments. Besides, the model predicts the formation of other species with a concentration below the detection limit of the APSIS MS measurements, *e.g.* most C5 and C6 species, especially benzene.

The mole fractions (except for N_2 and CH_4) were summed by block. In each Cx block, the distribution of the results is expressed by a violin plot, whose widths at different mole fraction values show the corresponding probability density (Fig. 4). Experimental results from the 7 sccm APSIS experiments [28] have been overlaid for comparison. The experimental mass spectrum intensities have been divided by their relative (to N_2) ionization cross-sections, estimated according to Eq. (16), *i.e.* 3, 4 and 5 for the C2, C3 and C4 blocks, respectively. Note that the Cx ($x \geqslant 2$) abundances follow a powerlaw distribution, as described by Dobrijevic and Dutour [53].

The simulation predictions are in good agreement with the APSIS MS measurements (Fig. 4), except for the C2 block, for which the large measurement uncertainties of the intensities on the N_2 peak shoulders [28] have to be considered. Note that this fair agreement also somewhat results from the large uncertainty on the model predictions.

In the reference simulation, radicals account for about one third of the total mass of products at stationary state. Thus, the simulated mass spectra, ignoring radicals, can only be compared to the APSIS MS on a qualitative or semi-quantitative basis (see Fig. 5). Except for the C2 block, the major bands in the experimental spectrum are well covered by the 95% confidence intervals of the simulated MS (the red shaded area in Fig. 5). However, the mean of the simulated spectrum is not in satisfactory agreement with the experimental spectrum: it underestimates the production of saturated C3 and C4 MS fragments and overestimates that of unsaturated C4 fragments. In the database used to build the spectra, the major fragmentation patterns of hydrocarbons might change the number of heavy atoms, but have a strong tendency to preserve the saturation state. For instance, the main fragment of C_3H_8 is at *m/z* 29 (C_2H_5) *vs.* 30 (C_2H_6), that of C_4H_{10} is at *m/z* 43 (C_3H_7) *vs.* 44 (C_3H_8), and for the unsaturated species, that of C_4H_4 is at *m/z* 52 *vs.* 58 (C_4H_{10}). Without considering specific details, one can conclude from this comparison that the experiment and simulation differ mostly by their production in saturated species.

The main causes of this discrepancy could be:

- **incompleteness of the reaction scheme**: an exhaustive search has been performed for the construction of the reaction scheme. Up to now, most C3-producing reactions have been included in

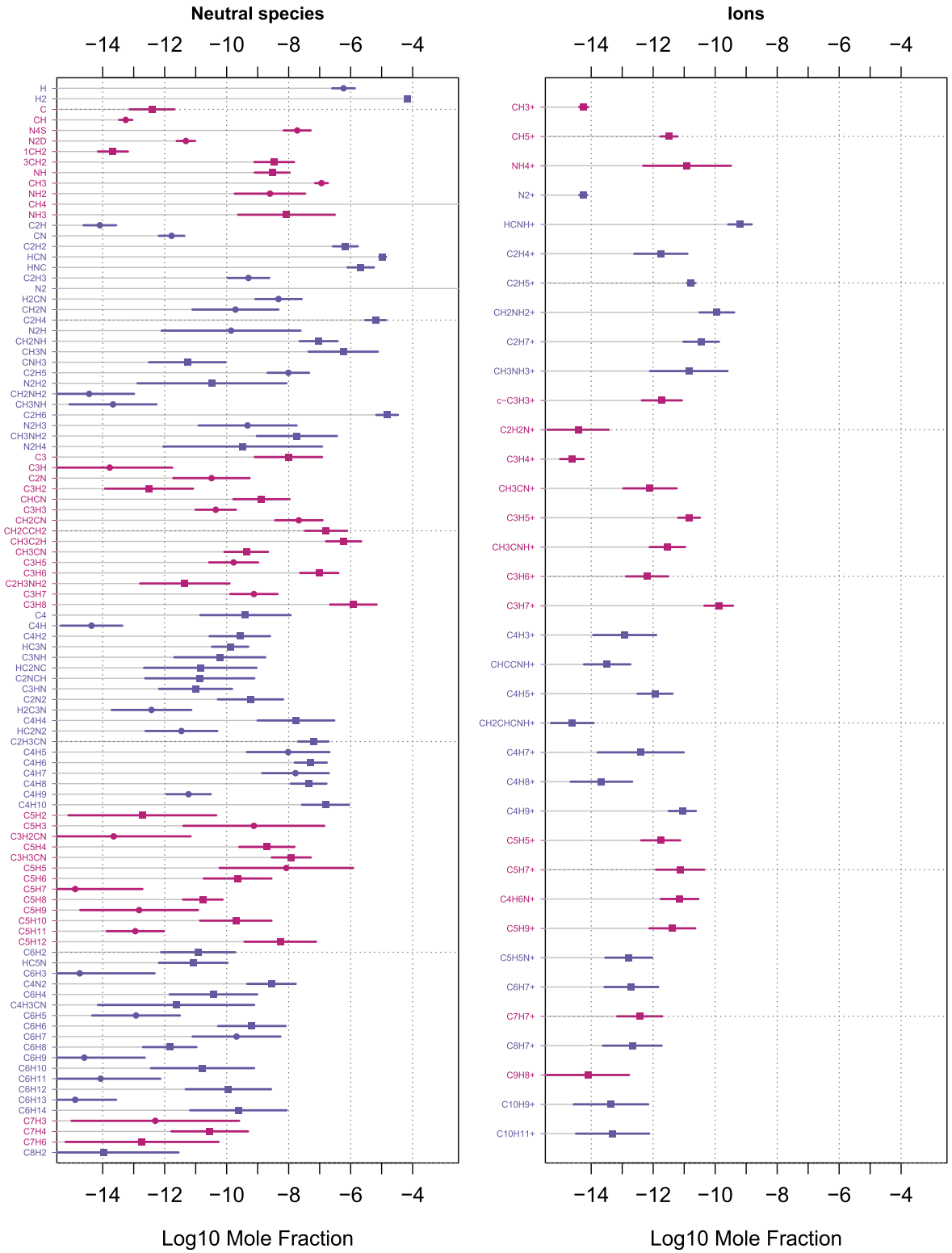

Fig. 3. Mole fractions (normalized to N_2) of neutral species (left panel) and ions (right panel) at the stationary state for the 500 runs of the 1-cell model with all uncertain parameters. The species are sorted downwards by increasing mass. Only species with an average mole fraction above 10^{-15} are represented and CH_4 has been left out of the graph for legibility: its Log10 Mole Fraction is -0.9545 ± 0.0001. Cx blocks are materialized by alternating colors. Neutral species with even/odd electron counts are marked by a square/circle symbol. Error bars cover a 95% confidence intervals.

the model, while saturated C3 species are still not satisfactorily simulated. Moreover, it is unlikely that missing reactions, randomly taken for each reaction type, could result in a systematic underestimation of saturated species,

- **oversimplification of the reactor geometry**: we considered the effect of a dark zone (the region in the reactor not or weakly irradiated) by running the model without irradiation but with a gas inflow composition identical to that of the stationary state

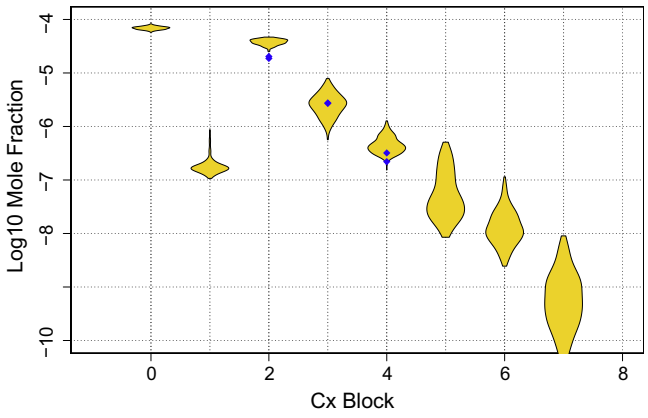

Fig. 4. Violin plots of the mole fractions of the Cx blocks for the reference simulation, excluding He, N_2 and CH_4. Blue points represent the corresponding experimental values corrected for ionization cross-sections. (For interpretation of the references to colour in this figure caption, the reader is referred to the web version of this article.)

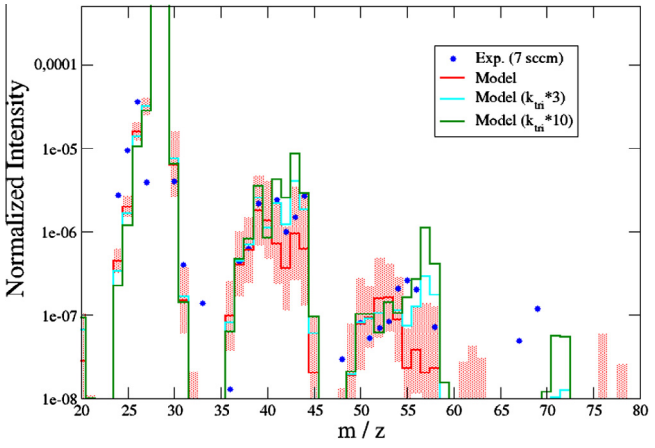

Fig. 5. Simulated neutral mass spectra (solid lines) of the reference case (red) compared to *in situ* gas phase MS in an APSIS experiment at 7 sccm (blue points). Additional simulations with trimolecular rate constants multiplied by a factor of 3 (cyan) and 10 (dark green) are also represented. The MS intensities are normalized with respect to that of N_2. The 95% confidence interval of the simulated reference spectrum is shown by shaded area. (For interpretation of the references to colour in this figure caption, the reader is referred to the web version of this article.)

gas outflow in the reference case. The gas inflow models the non or weakly irradiated part of the reactor, where reactive species other than N_2 and CH_4 are supplied by transport/diffusion. The stationary state of this test case is little shifted from the reference case, demonstrating, at least, that the basic growth scheme would hardly change in the dark zone of the reactor,

- **chemistry taking place in the capillary between the reactor and the mass spectrometer**: radicals and ions (about one third of the total mass of products) pumped into the capillary cannot qualitatively change the gas composition before reaching the mass spectrometer. This was shown by another test case, where we let the stationary state reactive gas of the reference case react until equilibrium in a closed box, without irradiation. In this case, radicals and ions have infinitely long time to combine with each other and be recombined with electrons, no matter whether catalyzed by the capillary stainless steel surface or not. In these conditions, saturated species concentrations are increased by at most 40%, still far from the observed difference between the experimental and simulated spectra. However, the increase of saturated species concentration resulting from radical recombination in this test case, points out that higher radical recombination rates would lead to a better reproduction of saturated species,
- **wall effects**: how could radical recombination rates be higher than in our reference model? It is unlikely due to homogeneous trimolecular reactions, since, although globally known with large uncertainty, their rate constants could hardly be *systematically* underestimated. Therefore, we may only consider heterogeneous catalysis, most probably on the reactor stainless steel walls, as detailed below.

Radicals and ions can be efficiently adsorbed or chemisorbed on stainless steel walls and undergo further chemistry. For instance, it has been observed that NH_3 can be generated in this manner by successive hydrogenation of atomic nitrogen and N-containing radicals [54]. In their laboratory simulation experiments of Titan's ionospheric chemistry Thissen et al. [26] concluded that surface effects were responsible for an excess production of NH_3 and HCN. Radicals recombination on the wall of the antechamber of the INMS mass spectrometer has been retained to explain the discrepancy between measured concentrations of C_6H_6 along the trajectory of the spacecraft in Titan's atmosphere [11]. Overall, wall effects in CH_4/N_2 plasmas are very complex and are the subject of ongoing studies [55].

Gorodetsky et al. [56] measured a CH_3 recombination coefficient of 3×10^{-4} on stainless steel at 300 K. According to this value, the reaction rate of CH_3 recombination on stainless steel is one to two orders of magnitude below that of the homogeneous rate. They determined also the temperature dependency of the rate constant, usually more reliable than its absolute value. They showed that recombination is accelerated about 10 times as temperature increases by 10 K. This high sensitivity may make the APSIS recombination rate highly uncertain, since the temperature during the experiments is not regulated. In addition, the large uncertainty usually associated with measurements of heterogeneous reaction rates and the existence of multiple radical recombinations on the reactor's wall should also be considered. The large uncertainties prevent us from making a quantitative comparison of the contributions of the homogeneous and the heterogeneous radical recombinations, but it cannot be ruled out that heterogeneous recombinations have a comparable, or even larger contribution than the homogeneous ones.

Without detailed reaction rate constants, it is difficult to model heterogeneous recombination explicitly without introducing adjustable parameters in the model [54]. In order to account for heterogeneous recombination in the present model, we made simulations where all the homogeneous trimolecular rate constants were multiplied by a factor 3 or 10 (cyan and dark green solid lines in Fig. 5, respectively). In the case of the factor 3, the unsaturated part of the C3 and C4 bands decreases slightly and their saturated parts increase significantly, by a factor about 3, leading to a better agreement of the C3 and C4 blocks. When trimolecular rate constants are 10 times larger than in the reference case, one gets an overestimation of the saturated part.

We observe that faster trimolecular recombination produces more saturated species, at the expense of unsaturated species. Unsaturated species play a major role in the growth without "heterogeneous recombination" included in the model, and their preponderance over saturated ones, not observed in the experiments, can be well compensated in the model by "heterogeneous recombination" that consumes unsaturated species and produces saturated ones. This is a strong indication of the contribution of heterogeneous reactions in the laboratory simulation setups of atmospheric chemistry, such as the APSIS reactor.

3.1.2. Uncertainty analysis

Uncertainty analysis for simulations of N_2/CH_4 plasmas were provided for Titan's atmosphere by Hébrard et al. [38,32] and Peng et al. [39] for neutral species predicted by a neutral model and by Carrasco et al. [34,42] and Plessis et al. [25] for ions predicted in a fixed neutral bath ionospheric model. The impact on predictions uncertainty of a fully coupled ion–neutral chemistry is assessed here for the first time. A particular concern was resulting from the introduction in the model of the exhaustive database of dissociative recombination branching ratios (with large uncertainties) of Plessis et al. [23] and its strong coupling with the neutral chemistry [25], and also from the large uncertainties in the branching ratios of the photolysis of CH_4 at most wavelengths covered by the DISCO spectrum [33,28].

In the following, we discuss the uncertainty factors of the mole fractions in these various models. These are defined as $F_i = \exp(u_{\log y_i})$, where $u_{\log y_i}$ is the standard deviation of the logarithm of the mole fraction y_i of species i, estimated on the Monte Carlo sample. If the distribution of y_i is lognormal, then one has about 95% probability for the mole fraction to be in the interval $\left[\tilde{y}_i/F_i^2, \tilde{y}_i \times F_i^2\right]$, where $\tilde{y}_i = \exp(\overline{\log y_i})$ is the geometric mean. As a thumbrule, mole fractions with uncertainty factors of about 3 are known up to an order of magnitude.

Empirical Cumulated Density Functions (ECDF) of the uncertainty factors on the stationary mole fractions of neutrals and ions of the APSIS simulation are reported in Fig. 6, where we display also the ECDF for the uncertainty factors obtained in Hébrard et al. [32] for neutral species at 1200 km in Titan's ionosphere, and by Carrasco et al. [34] at the same altitude for a ionic model with fixed neutral bath. The uncertainty factors for both ions and neutrals are globally increased when compared with their uncoupled versions. The effect is stronger for ions, a direct consequence of their production from neutral species with uncertain densities, whereas these densities were fixed in Carrasco et al. [34]. These authors ranked this uncertainty source as a major one in the uncertainty budget of predicted ions densities, which is confirmed by the present study. Globally however, 60% of the ions are predicted with smaller uncertainty than neutrals, an effect of the reaction rate constants of ionic processes being usually measured with better precision.

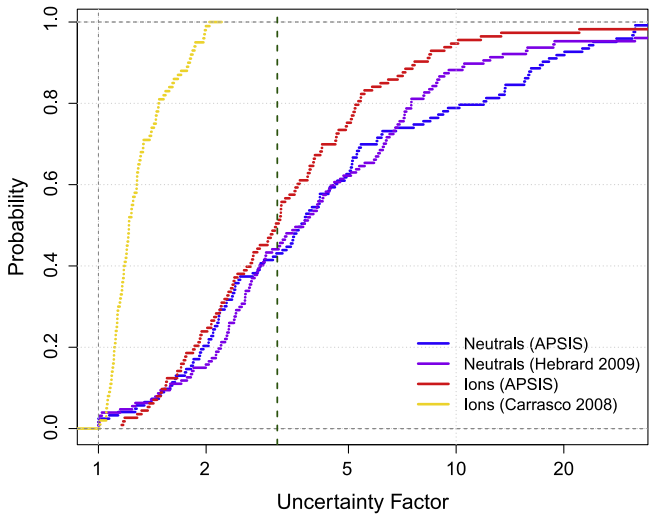

Fig. 6. Empirical Cumulated Density Functions of the uncertainty factors, in log scale, of the neutrals (blue) and ions (red) concentrations at the stationary state of the APSIS model. The uncertainty factors of the simulated neutral species in Titan's atmosphere at 1200 km from Hébrard et al. [32] (cyan) and ions from Carrasco et al. [34] (pink) are reported for comparison. The heavy dash vertical line marks the "up to one order of magnitude" 95% uncertainty range. (For interpretation of the references to colour in this figure caption, the reader is referred to the web version of this article.)

The ECDF for 70 % of the lower uncertainty factors of neutrals mole fractions is indistinguishable between the present model and the neutral model of Hébrard et al. [32], and substantially larger uncertainty factors occur in the present model for the remaining 30%. At this level it is difficult to identify the cause of this enhanced uncertainty factors: working at room temperature in APSIS should avoid the large temperature extrapolation uncertainty in Titan's ionospheric models [32], but on the other hand, working at higher pressures favors the trimolecular reactions, which rate constants have large uncertainty factors (F_k from 2 to 10).

The uncertainty factors on the stationary mole fractions of neutrals and ions are presented in Fig. 7 as a function of their molecular mass, and the species with the largest uncertainty factors have been tagged. As in Hébrard et al. [38] and Peng et al. [39], we observe that uncertainty has the trend to increase with molecular mass, which may be roughly interpreted as the accumulation of uncertainty along growth pathways (see detailed discussion in Peng et al. [39]). For species like N_2H, N_2H_2 and N_2H_4, very large uncertainty factors are due to their production from NH_2, itself issued from the dissociative recombination of $CH_2NH_2^+$, for which there are no data on the branching ratios. Similarly, for most other tagged species, we find unknown dissociative recombination branching ratios as a key factor. For ions, large uncertainties can be also traced back to large uncertainty on some dissociative recombination branching ratios.

3.1.3. Sensitivity analysis

3.1.3.1. Main contributions to prediction uncertainty. To better understand the large uncertainty factors in the predictions of the present model, we analyze their variance with regard to the main types of reactions. For this, we calculate the portion of the total variance explained by each type of process: photolysis, reactions (neutral and ionic bi- and trimolecular), and dissociative recombination, by running simulations where a single type of process is treated as uncertain, while the others have fixed rate constants.

The results are summarized in Fig. 8, where we report, for each type of process, the frequency of it being the dominant contributor to the output variance of the stationary mole fraction of neutrals and ions. For reference, we plot also the occurrence frequency of each reaction type in the model (see Section 2.2). The scores for neutrals and ions are remarkably correlated to this occurrence frequency, with minor deviations for both categories. The contribution of bi- and trimolecular reactions to the mole fractions variance in the reference case is dominant, from nearly 80% for neutrals to 60% for ions. Dissociative recombination contribute significantly, with a score of about 30% for both ions and neutrals, slightly lower than the occurrence frequency of this process. Photodissociation and photoionization appear as negligible for neutral species, in accordance to the weak number of these processes in the model, but have an enhanced contribution to 15% of the cases for ions, for which photoionization is a necessary initiation pathway. It is to be noted that the highly uncertain representation of the photolysis branching ratios of methane and other photoabsorbers (see Section 2.2.1) does not impact significantly on the uncertainty budget of this simulation. Similarly, the contribution of dissociative recombination does not seem to be enhanced by the coupled chemical scheme. For both photolysis and dissociative recombination, the care taken in the representation of branching ratios as sum-to-one variables is certainly repaid for in the uncertainty budget.

3.1.3.2. Key reactions identification. Beyond the overall view provided by the previous variance analysis, we aim at the identification of *key reactions*, defined as the reactions that contribute significantly to the model output uncertainty [57]. A key reaction

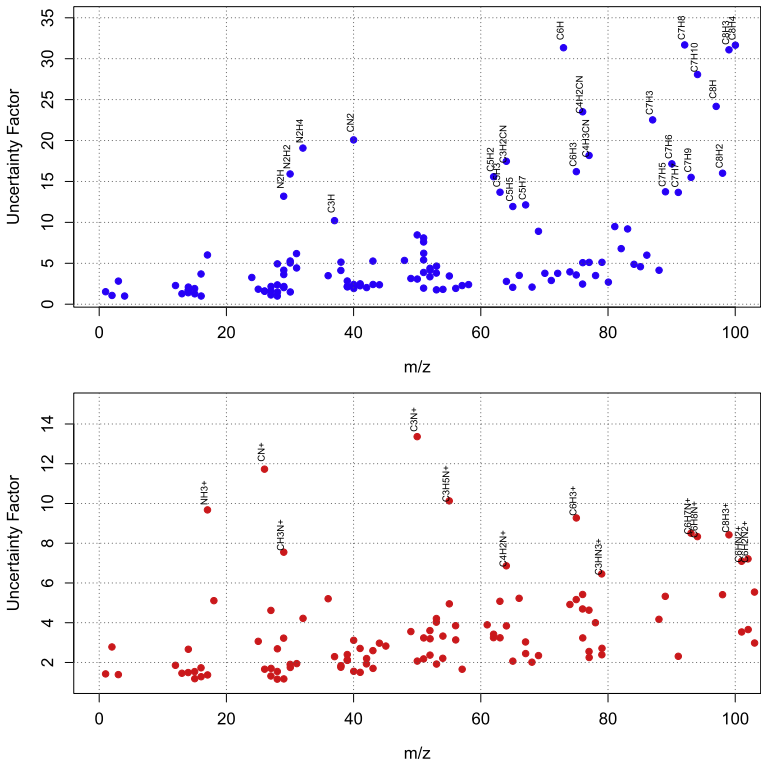

Fig. 7. Uncertainty factors of the neutrals (blue, upper) and ions (red, lower) concentrations at the stationary state of the 1-cell model with all uncertain parameters. The names of the species with the largest uncertainty factors are reported. (For interpretation of the references to colour in this figure caption, the reader is referred to the web version of this article.)

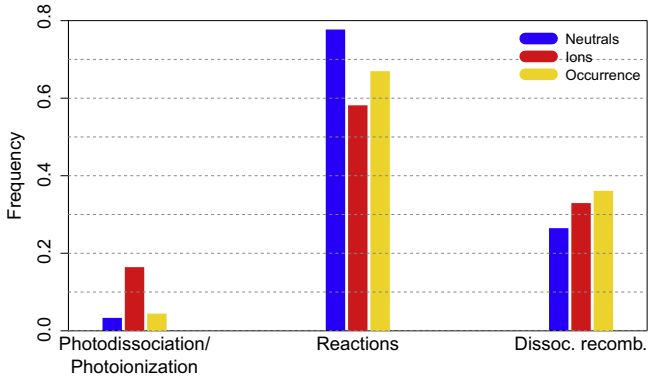

Fig. 8. Frequency for each reaction type as the major contributor to the variance of the mole fractions of neutral species (blue) and ions (red). The occurrence frequency of each reaction type in the database is reported for reference (gold). (For interpretation of the references to colour in this figure caption, the reader is referred to the web version of this article.)

might appear for two different reasons: (i) reactions that have a strong effect on the mass flux in a reaction network; (ii) reactions with a rate constant in need of further study to improve the prediction precision of model outputs; or both. A few recent studies identified the *key reactions* of complex chemical networks by computing the rank correlation coefficients between rate constants and species concentrations from the Monte Carlo samples [32,39,57,58]. To select their key reactions, Hébrard et al. [32] and Peng et al. [39] retained reactions presenting correlation coefficients larger than 0.2 in absolute value with the mole fractions of more than 15 species. We adopted the same procedure, which produced 14 key reactions, as listed in Table 2 with the corresponding number $N_>$ of above-threshold species, and reaction rate uncertainty factors F_k estimated from the input Monte Carlo sample.

Table 2
Key reactions identified for the reference simulation, their rate constant uncertainty factor F_k in the conditions of the reference APSIS simulation, the corresponding number $N_>$ of species used for selection, and their S score (see text). Bold characters indicate the maximum in each column.

Reaction	F_k	Scores	
		$N_>$	S
$H + C_2H_3 \longrightarrow C_2H_2 + H_2$	3.9	**55**	6.9
$H1 + C_2H_4 \longrightarrow C_2H_5$	2.0	48	6.6
$H + CH_3 \longrightarrow CH_4$	2.9	39	6.9
$CH_2NH_2^+ + e^- \longrightarrow {}^3CH_2 + NH_2$	5.2	32	7.4
$CH_2NH_2^+ + e^- \longrightarrow {}^1CH_2 + NH_2$	5.2	26	7.1
$CH_2NH_2^+ + e^- \longrightarrow HCN + H_2 + H$	5.2	19	<3.0
$N_2^+ + CH_4 \longrightarrow CH_2^+ + H_2 + N_2$	3.6	31	**8.1**
$N(^2D) + N_2 \longrightarrow N(^4S) + N_2$	2.1	30	5.0
$N_2 + h\nu \longrightarrow N_2^+ + e^-$	<1.1	19	4.1
$N_2 + h\nu \longrightarrow N(^4S) + N(^2D)$	<1.1	17	4.4
$CH_4 + h\nu \longrightarrow CH^+ + H_2 + H + e^-$	1.4	17	3.7
$C_2H_5^+ + HCN \longrightarrow HCNH^+ + C_2H_4$	1.2	17	3.1
$CHCN + CHCN \longrightarrow C_4N_2 + H_2$	**10.0**	17	6.2
$N(^4S) + CHCN \longrightarrow C_2N_2 + H$	2.9	16	3.3

In order to confirm this selection, we estimated the global influence of a reaction through the sum of the squares of its correlation coefficients with the stationary mole fractions of all species. We define the score S_j of the jth reaction as

$$S_j = \sum_{i \in \{\text{species}\}} r_{ij}^2, \tag{19}$$

where r_{ij} is the rank correlation coefficient between the i^{th} species and the corresponding reaction rate. The scores are reported in Table 2. All the reactions with the higher S scores are also in the top list selected by the other method, and only the scoring order is slightly perturbed.

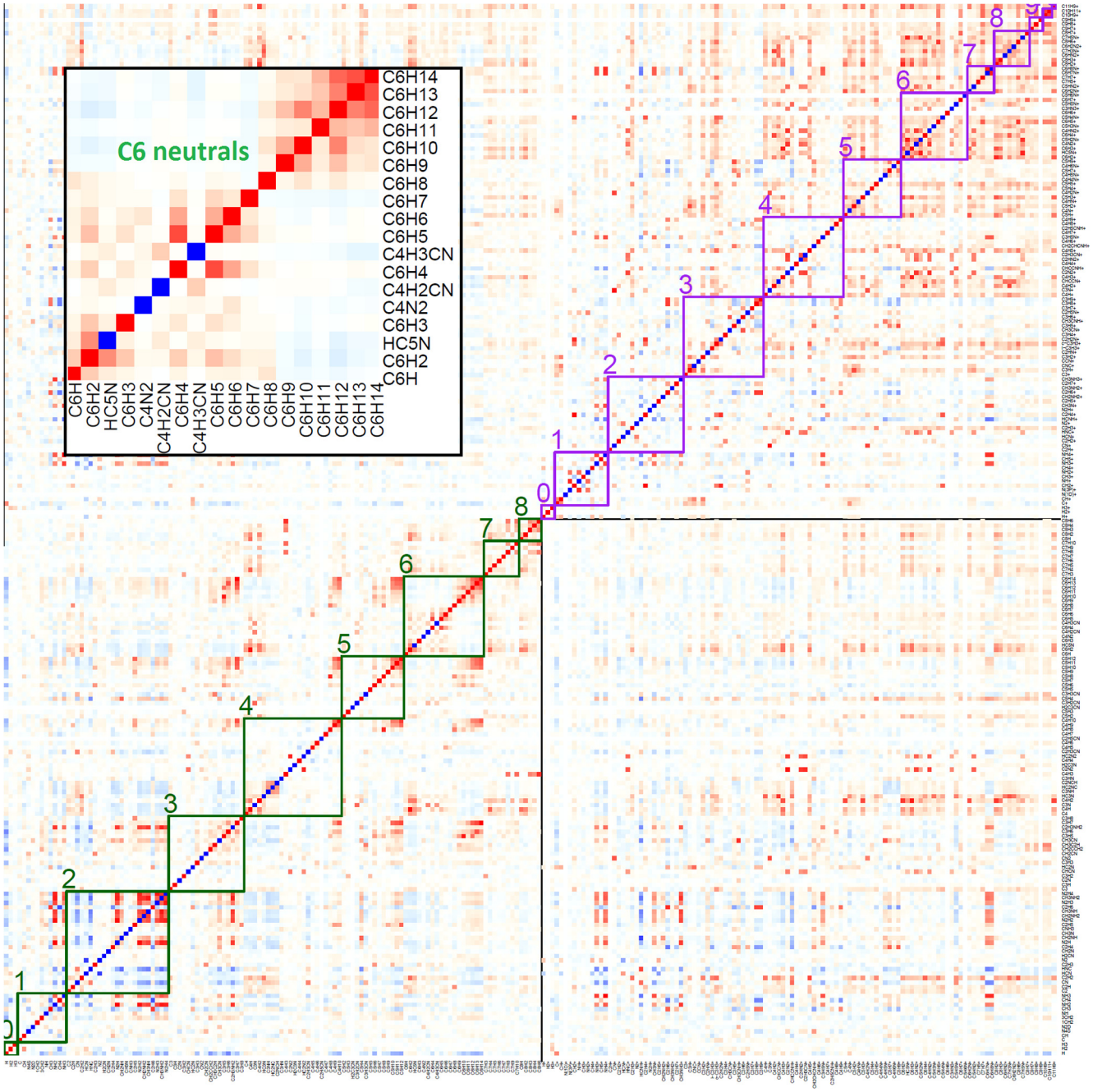

Fig. 9. Correlation matrix of Monte Carlo stationary state mole fractions. Species are sorted: 1/ by charge (neutrals in the bottomleft, ions in the topright; the black lines in the lower triangle mark the limit between neutral species and ions); and 2/ by increasing mass. The Cx blocks are overlined and labeled by the number of heavy atoms (darkgreen for neutrals; purple for ions). Correlation coefficients from −1 to 1 are denoted by pixels whose color gradually changes from blue (−1) to red (1) via white (0), except on the diagonal, where the color code is red for hydrocarbons and blue for N-bearing species. The inset is the C6 block of neutral species. (For interpretation of the references to color in this figure legend, the reader is referred to the web version of this article.)

The list of key reactions is heterogeneous in the sense that, as stated above, it contains reactions with high uncertainty factors (above 3) and reactions with small uncertainty factors (below 1.5).

The first ones (*e.g.* $H + C_2H_3 \longrightarrow C_2H_2 + H_2$; $F_k = 3.9$) contribute importantly to the uncertainty budget of the simulation, and more accurate estimations of their rate constants would have a positive impact on prediction precision at a global level. In the same category, $N_2^+ + CH_4 \longrightarrow CH_2^+ + H_2 + N_2$ ($F_k = 3.6$) is a minor channel of a reaction with a rather accurate global rate constant ($F_k = 1.15$) which would benefit of a better evaluation of its branching ratio ($b = 0.08 \pm 0.08$; Carrasco et al. [42]). This global reaction is an important step in the formation of primary ions from CH_4. Another example is the dissociative recombination of $CH_2NH_2^+$ (the third most abundant ion in the reference simulation after $HCNH^+$ and $C_3H_7^+$, see Fig. 3), for which both the rate constant and the branching ratios are unknown. The strong impact of this process on some species has been noted in Section 3.1.2. This hampering lack of data was also mentioned by Yelle et al. [17] for a Titan ionospheric model. The branching ratios of this reaction determine the portion of $CH_2NH_2^+$ converted to CH_2NH, methanimine, a possible precursor of tholins [59].

In the second group of reactions, one has for instance the photolysis of N_2. This process is essential to the formation of ions and

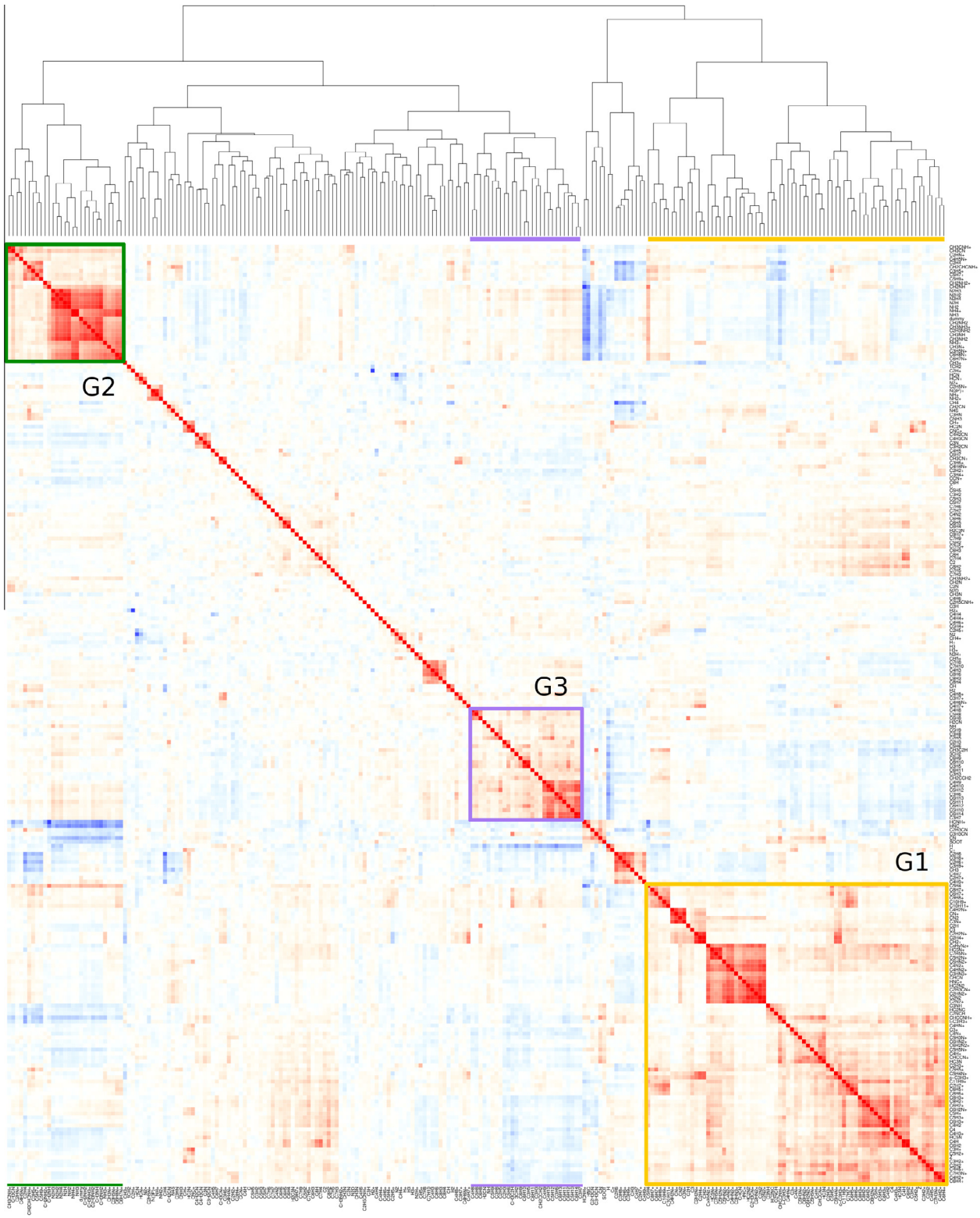

Fig. 10. Heatmap of the outputs correlation matrix. Correlation coefficients from −1 to 1 are denoted by squares whose color gradually changes from blue (−1) to red (1) via white (0). The colored borders (orange, purple, green) delimit the clusters discussed in the text. The hierarchical tree is displayed at the top of the matrix, and the relevant clusters G1, G2 and G3 are underlined by color. (For interpretation of the references to colour in this figure caption, the reader is referred to the web version of this article.)

integration of N in the system, but it is rather hopeless to expect a reduction of its already small uncertainty factor ($F_k < 1.1$).

It is striking that two trimolecular reactions appear at the top of the list. In the model of Titan's upper atmosphere [32], most key processes were photolysis and bimolecular reactions, and only one trimolecular reaction was found to be influential, at low altitude. Indeed, trimolecular reactions are influential in the APSIS model because their rate is enhanced by the comparatively high pressure in the reactor. We note also that, despite the sizable uncertainty on its rate constant ($F_k \simeq 7$), $H + CH \rightarrow C + H_2$, the

most influential reaction in the model of Titan's upper atmosphere reported by Hébrard et al. [32], is not identified as a key reaction for the present simulation, although we will see that it reappears in the list for simulations in Titan-like conditions (Table 4).

Two reactions involving CHCN appear in the list. This species plays a key role in the formation of C_2N_2 and C_4N_2. An issue with its chemistry has been raised by Imanaka and Smith [27], and we report the discussion to Section 3.2.

3.1.4. Species correlation analysis

Although we know in every detail the reaction scheme of the model, its complexity and the high uncertainty on many kinetic parameters make it delicate to predict the main pathways without a numerical search. We propose here to exploit the sample of species mole fractions generated for uncertainty/sensitivity analysis to gather information on the relationships between species through correlation analysis.

The correlation coefficient between the stationary mole fractions of two species calculated from the MCUP outputs sample contains information on the way these species respond to a global perturbation of the system (*i.e.* random variation of all the rate constants). Considering a scheme with a single reaction, *e.g.* $R_1 + R_2 \longrightarrow P_1 + P_2$, and taking the concentrations at a given time, one expects a strong (unit) positive correlation between reactants $r_{R_1R_2} = 1$ and between products $r_{P_1P_2} = 1$, and a strong anticorrelation between reactants and products $r_{R_iP_j} = -1$. For more complex systems, the correlation strength depends on the structure of the reaction network between two species, and on the relative effects of various reaction rate constants on those species.

3.1.4.1. Inter-species correlation matrix. In a first step, we consider the inter-species correlation matrix, and more particularly examine the presence of structures and their link to the underlying chemical scheme. The rank correlation matrix of mole fractions at stationary state for the APSIS simulation is shown in Fig. 9, where the species are sorted (i) by charge; and (ii) by mass. The Cx blocks are overlined and labeled by the corresponding number of heavy atoms.

At the global scale, one observes that the neutrals and ions present rather different correlation patterns, with a massive inter-blocks correlation structure for the ions, whereas the correlation pattern seems more specific between neutral species. There is also a notable correlation pattern between neutrals and ions. The inter-ions structure is reminiscent of the inter-mass correlation matrix built recently by Westlake et al. [18] from the intensities of INMS ion data between 1200 and 2000 km, over a large sample of Cassini flybys. Westlake et al. [18] observed a block pattern in the matrix and linked it to molecular growth through the addition of C1 and C2 units.

If we enter into more details, we observe several features in the neutral and ion Cx blocks along the diagonal: some species within a Cx block form a red square, hinting to a similarity of their reactivity. The most striking example arises in the C6 neutral block (see the inset of Fig. 9), where two squares of red pixels are visible: a square in the lower left of the block, between C_6H and C_6H_7, relatively unsaturated species, and another in the upper right, between C_6H_8 and C_6H_{14}, relatively saturated hydrocarbons. Out of these two squares, there are off-diagonal light blue pixels, which indicate a negative correlation of species between the two squares. We interpret this pattern as revealing separate and competing pathways for unsaturated and saturated species in this block. This pattern is present in other blocks, although with less clarity.

Inter-blocks correlation may provide information on molecular growth. Highly positive correlation between two species with different heavy atom numbers may not only suggest a similar formation pathway, but also a direct link by a reaction realizing molecular growth, *i.e.* the addition of small chemical units. Positive inter-block correlations are obvious between most saturated heavy neutrals, or between most unsaturated heavy neutrals. They are more common between heavy ions, either between unsaturated ones or between saturated ones.

In general, unsaturated and saturated ions are positively correlated to their respective neutral counterparts. Saturated species have negative correlations with unsaturated ones, regardless of whether they are neutrals or ions. Given all that, saturated and unsaturated species are likely to be formed through distinct growth/formation pathways.

3.1.4.2. Cluster analysis. Except for simple chemical schemes, information based on inter-species correlation is too condensed to enable the reconstruction of a detailed mechanism, but we can use it as a basis for a cluster analysis, grouping together species responding similarly to the perturbation. Species within a cluster are then assumed, through their similarity, to be part of a common pathway. For instance, in the case of molecular growth which is our main target here, we expect that all species depending on a given growth unit will share a cluster, possibly with this unit.

The clustering analysis was done using the *heatmap* function in R [60], which builds a hierarchical clustering tree. The *heatmap* function plots a matrix, with rows and columns reordered to match the dendrogram plotted in the margins. The dendrogram is obtained by a hierarchical clustering algorithm *hclust*. The clusters are built iteratively, starting by one matrix row (column) per cluster. We used the default agglomeration method in the *hclust* function, the *complete linkage* method, which finds and groups similar clusters [61]. The correlation matrix (Fig. 9) reordered by the hierarchical clustering method is displayed in Fig. 10.

We focus on the largest clusters of positively correlated species. The three main ones (named G1, G2 and G3), totaling 133 species over the whole 244, are emphasized in the heatmap. The list of species in these clusters is provided in Table 3.

A large cluster of 74 positively correlated species (orange border) is seen at the bottom right. In this group, named G1, 77% of

Table 3
Species lists, sorted by increasing molecular mass, from the three clusters identified in Fig. 10. The species with the highest score *S* (see text) in each group are reported in bold.

Cluster name	Species in cluster
G1	CH_2^+, C_2H, C_2H_2, CN^+, HNC^+, $C_2H_3^+$, $C_2H_4^+$, C_3, C_3^+, C_3H^+, $C_3H_2^+$, CHCN, $1-C_3H_3^+$, $c-C_3H_3^+$, CN_2, $C_2H_2N^+$, C_4, C_4H^+, C_4H, C_3N^+, C_4H_2, $C_4H_2^+$, C_3NH, HC_2NC, C_2NCH, $CHCCN^+$, HC_3N, $C_4H_3^+$, C_2N_2, $C_2N_2^+$, $CHCCNH^+$, HC_2N_2, $C_2H_3CN^+$, $C_2HN_2^+$, $C_4H_5^+$, $C_4H_9^+$, C_5H^+, C_4N^+, $C_5H_2^+$, C_4HN^+, $C_5H_3^+$, C_5H_4, $C_4H_2N^+$, $C_5H_5^+$, $C_6H_2^+$, C_6H_2, HC_5N^+, $C_6H_3^+$, HC_5N, $C_5H_2N^+$, $C_4N_2^+$, $C_6H_4^+$, $C_4HN_2^+$, $C_5H_3N^+$, $C_6H_5^+$, $C_5H_4N^+$, $C_6H_7^+$, $C_3HN_3^+$, $C_5H_5N^+$, $C_6H_2N^+$, $C_5HN_2^+$, $C_7H_7^+$, $C_8H_2^+$, $C_8H_3^+$, $C_6HN_2^+$, $C_7H_3N^+$, $C_6H_2N_2^+$, $C_8H_6^+$, $C_8H_7^+$, $C_7H_5N^+$, $C_9H_8^+$, $C_{10}H_9^+$, $C_{10}H_{11}^+$, $C_{11}H_9^+$
G2	CH_3^+, NH_2, NH_3, NH_3^+, NH_4^+, C_2H_4, CH_2NH, N_2H, CH_3N^+, $CH_2NH_2^+$, N_2H_2, CH_2NH_2, CH_3NH, N_2H_3, CH_3NH_2, N_2H_4, $CH_3NH_3^+$, C_2HN^+, CH_3CN, $C_3H_5^+$, CH_3CNH^+, $C_2H_3NH_2$, CH_2CHCNH^+, $C_3H_5N^+$, $C_4H_5N^+$, $C_5H_7^+$, $C_5H_9^+$, $C_6H_7N^+$, $C_6H_8N^+$
G3	$^3CH_2$, NH, C_2H_3, H_2CN, C_2H_5, HCNH, C_3H_3, CH_3C_2H, CH_2CCH_2, C_3H_5, C_3H_6, C_3H_7, C_3H_8, $C_4H_7^+$, C_4H_8, C_4H_9, C_4H_{10}, C_5H_6, C_5H_8, C_5H_9, C_5H_{10}, C_5H_{11}, C_5H_{12}, C_6H_8, C_6H_9, C_6H_{10}, C_6H_{11}, C_6H_{12}, C_6H_{13}, C_6H_{14}

the members are ions and 47% are N-bearing species. At the top left of the heatmap, another cluster (G2 – green square) contains 29 species, and is composed for 55% of ions and 83% of N-bearing species. The third remarkable cluster, G3, is located near the middle of the heatmap (purple border) and contains 30 species. It is composed for 87% of neutral hydrocarbons.

The mass distribution and van Krevelen diagram [62,63] for the three groups are given in Fig. 11. The three clusters contain heavy species, but the G1 cluster contains the largest proportion of the heavier ones. At the compositional level, there is a neat discrimination of the three groups in the (N/C;H/C) space: the G1 cluster contains mostly H-poor (H/C$\leqslant$ 1) species, the G3 cluster is essentially composed of rather saturated hydrocarbons (H/C>1), while the G2 cluster contains more saturated species than the first one.

As we did for key reactions, we define within each cluster a score S for each species according to its cumulative squared correlation coefficient with the other species in the cluster (cf. Eq. (19)).

Cluster G1. The species with the highest score within G1 is by far C_2H_2 ($S = 15.2$).

All of the species in the cluster are rather unsaturated and most of them are ions. N-bearing species in this cluster are secondary products of the hydrocarbons discussed next. Considering these features, as well as the mechanism of molecular growth by addition of small units discussed previously, we identified a growth pathway *through* the recursive addition of C_2H_2 by ion–molecule reactions. A typical pathway is

$$C_2H_2^+ \xrightarrow[-H]{+C_2H_2} C_4H_3^+ \xrightarrow{+C_2H_2} C_6H_5^+ \xrightarrow[-H]{+C_2H_2} C_8H_6^+. \quad (20)$$

In the chemical scheme, C_2H_2 can be added to most ions with a sizable rate constant, while increasing the degree of unsaturation in the products. In their synchrotron irradiation study of different $N_2/CH_4/C_2H_x$ gas mixtures, Thissen et al. [26] have observed that C_2H_2 is the most efficient C2 compound to promote ions growth.

On the other hand, the importance of the ion chemistry does not mean that the contribution of the neutral chemistry is negligible. A neutral growth scheme was highlighted by Peng et al. [39]:

$$C_2H \xrightarrow[-H]{+C_2H_2} C_4H_2 \xrightarrow[-RH]{+R} C_4H \xrightarrow[-H]{+C_2H_2} C_6H_2, \quad (21)$$

where R represents various radicals. This scheme may also be typical for the production of unsaturated species, albeit a hydrogen

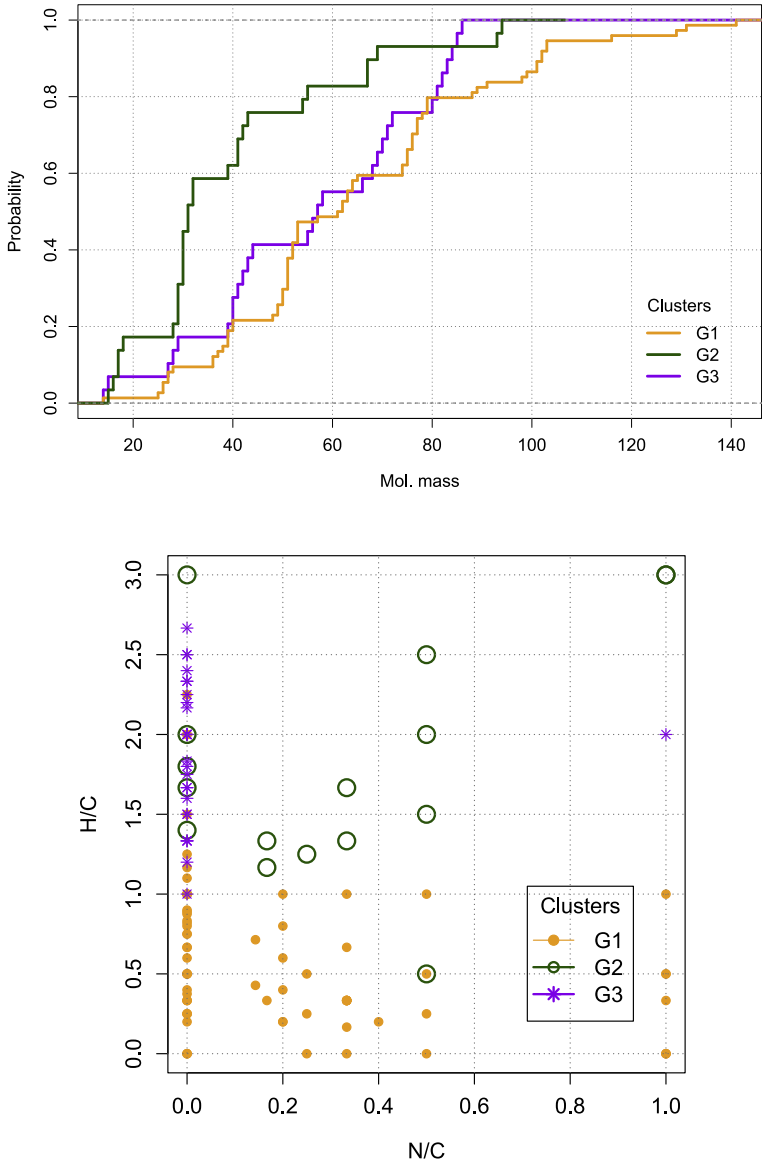

Fig. 11. Compositional analysis of the main clusters identified in Fig. 10: (top) molecular mass distribution; (bottom) van Krevelen diagram (this is a closeup on the densest zone for better legibility).

abstraction step is necessary to reactivate the intermediate. Otherwise 2 hydrocarbons of even hydrogen atom number, usually stable species, are not able to react with each other. Growth pathways by repeated addition of C_2H to form polyacetylenes as proposed in Ar/C_2H_2 plasmas [64], or studied in molecular jets [65], are found to be negligible in APSIS conditions, where the very low concentration of C_2H (Fig. 3) rapidly dampens this process.

Cluster G2. The species with the highest score within G2 is CH_3NH_2 ($S = 10.9$), with close scores for NH_2 ($S = 10.6$) and NH_3 ($S = 10.2$). Moreover, 83% of the species in this block are N-bearing ones. The cluster contains a major nitrogen fixation pathway [66]

$$CH_4 \xrightarrow[-H]{+N(^2D)} CH_2NH \xrightarrow[-R]{+RH^+} CH_2NH_2^+ \xrightarrow[-CH_2]{+e^-} NH_2 \xrightarrow{+CH_3} CH_3NH_2. \quad (22)$$

By analogy with the pathway involving C_2H_2, we observe also a minor growth pathway involving the repeated addition of C_2H_4 through ion–molecule reactions, *e.g.*

$$CH_3^+ \xrightarrow[-H2]{+CH_4} C_2H_5^+ \xrightarrow[-CH_4]{+C_2H_4} C_3H_5^+ \xrightarrow{+C_2H_4} C_5H_9^+, \quad (23)$$

that forms species more saturated than those in the G1 block. However, the importance of this pathway in hydrocarbon growth is quite limited. In the experiments by Thissen et al. [26], no significant effect was observed when adding C_2H_4 to a $N_2/CH_4/C_2H_2$ gas mixture, except for the increased abundance of $C_3H_5^+$. In fact, the rate constants of neutral growth reactions involving C_2H_4 are significantly smaller than those involving C_2H_2: for example, the rate constant at 300 K for the addition of C_2H_2 to C_4H is about 30 times larger than for the addition of C_2H_4.

Cluster G3. This cluster contains relatively saturated species, including the most saturated hydrocarbons. The species with the highest score within G3 is C_5H_{12} ($S = 6.8$), closely followed by C_3H_7 ($S = 6.3$). The former is a terminal product, whereas C_3H_7 appears as a hub within this cluster and enables the formation of heavy saturated species by addition to small radical units ($CH_3, C_2H_3, C_2H_5 \ldots$). Saturated hydrocarbons are usually formed by trimolecular reactions, preserving or decreasing the degree of unsaturation of the products. Note that trimolecular reactions involve quite often two radicals, whose concentrations are much lower than those of stable C2 species, such as C2H2. Thus, this cluster's pathways may not be as efficient in promoting molecular growth as those operating in the G1 group.

3.1.4.3. The pathways of molecular growth. To conclude this correlation analysis, the clusters G3 and G1 have been identified as strongly involved in the growth of saturated and unsaturated species, respectively. As previously discussed, they are in competition and a possible link between both groups is the ratio between C_2H_2 and C_2H_3 (in the G3 group), which are interconnected by reactions with H atoms.

In spite of the partition of the correlation matrix, interactions between the clusters discussed above, still exists, forming species of a degree of unsaturation between the typical cases and complexifying the growth scheme. However, considering the size of the clusters in the heatmap, the prominence of the G1 cluster is flagrant, and, in view of the importance of ion chemistry in the present simulation, the addition of C_2H_2 through ion–molecule reactions might be considered at the center of the growth scheme in APSIS conditions.

3.1.5. Impact study of physical conditions

Having highlighted the growth mechanism in the APSIS model, we explore the chemistry of the system in different physical conditions, in order to interpret other observations or experiments. To identify the effect of various physical factors, we design variants of the reference model with a single modified factor: irradiation spectrum, pressure, and temperature. The parameters for all simulations are gathered in Table 1.

3.1.5.1. Irradiation spectrum. We consider here simulations with monochromatic beams at 60 nm and 82 nm, as used by Imanaka and Smith [27] (the adopted 1 nm wavelength resolution does not enable to simulate their 82.5 nm). The simulations are performed with the same integrated photon flux as the reference one. Another simulation is performed with a proxy of the solar spectrum [67], again at the same integrated intensity as in the reference case. Monte Carlo samples of 150 runs were performed for each case.

For comparison with the reference (DISCO) case, we calculated methane consumption ratio ρ_{CH_4} and the ratios of the mole fractions of the modified simulation over the reference simulation and reported them in Fig. 12 for neutral species. The uncertainty on the ratios is obtained by combination of variance [68].

In the 60 nm case, $\rho_{CH_4} = 5\%$, about two orders of magnitude higher than the reference value (0.07 %, *cf.* Table 1). Moreover, the relative production of individual species increases with their molecular mass (Fig. 12 (top)). This increase is explained by the enhancement of ion chemistry: N_2 photolysis at 60 nm essentially produces N_2^+, which almost quantitatively ionizes methane through reactions

$$N_2^+ + CH_4 \longrightarrow CH_2^+ + H_2 + N_2, \quad (24)$$

$$N_2^+ + CH_4 \longrightarrow CH_3^+ + H + N_2, \quad (25)$$

and initiates the growth of hydrocarbon ions. This process has been identified as a key reaction for the APSIS simulation and its effect in promoting the growth through ion chemistry has also been highlighted in the literature [26,69].

Irradiation at 82 nm is less efficient than at 60 nm ($\rho_{CH_4} = 3.3\%$). Although at this wavelength N_2 is not ionized but produces N atoms, the direct production of CH_4 ionic photoproducts still benefits of more photons than in the wide DISCO spectrum. Furthermore, this wavelength is promoting the formation of N-bearing species (outlined by red squares in Fig. 12(middle)), in agreement with the experimental results of Imanaka and Smith [27].

In the conditions of solar-like irradiation (Fig. 12 (bottom)), the fraction of ionizing photons is considerably reduced, and the methane consumption drops to $\rho_{CH_4} = 0.008\%$ (Table 1). Besides, one observes a decrease of the relative mole fractions with mass. As the ionizing part of the spectrum is reduced, ion-promoted molecular growth is not efficient, considering the limited residence time in the reactor in this simulation. This also translates into a systematic tendency in each Cx block to have a reduction of the unsaturated species (red lines in Fig. 12 (bottom)).

Uncertainty analysis. The uncertainties on the stationary mole fractions for the 60 nm and solar irradiations are found to be little sensitive to the irradiation type. In Section 3.1.2, the contribution of the photolysis to the concentration uncertainties was shown to be minor. As long as the uncertainty introduced by the photolysis is not increased drastically, their total contribution to the uncertainty cannot be significant. In these two cases, the principal contribution of the photolysis stems from photoionization at 60 nm and photodissociation at Ly-α, respectively. The branching ratios at these two wavelengths are accurately measured (relative uncertainties below 20%). Therefore, the major uncertainty source remains neutral thermal reactions, and the concentration uncertainties are close to those in the reference case.

By contrast, the mole fractions uncertainty increases notably in the 82 nm case. At this wavelength, one is close to the lower extremity of the wavelength range covered by the representation

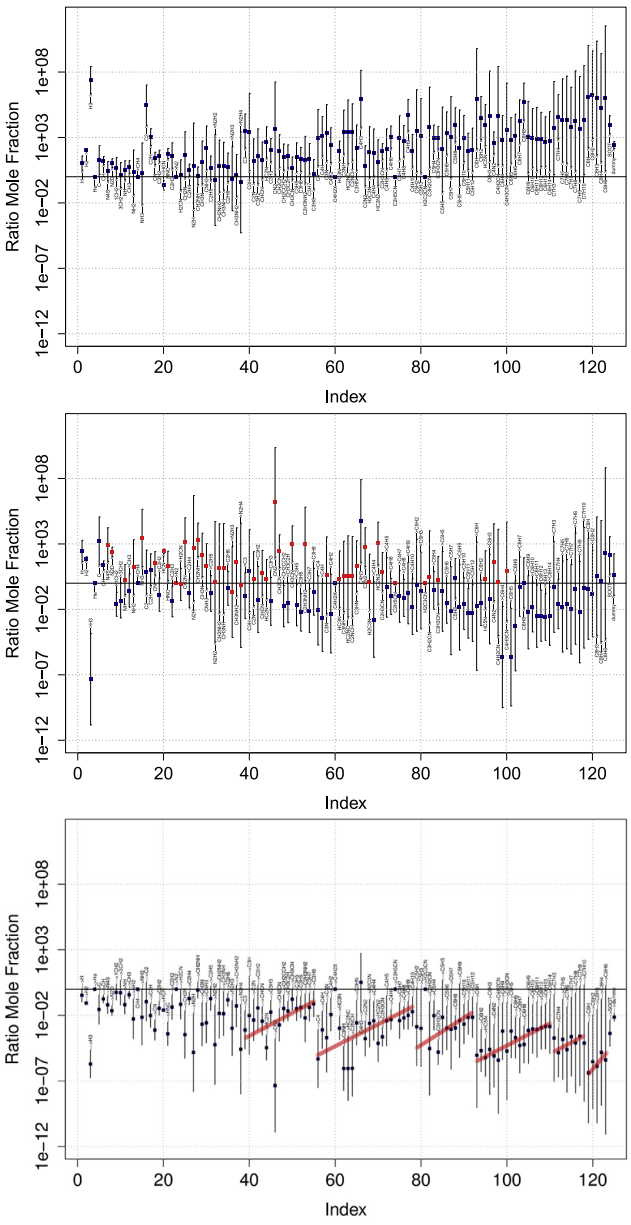

Fig. 12. Ratios of stationary concentrations of neutral species for different irradiation spectra to those in the reference model: (top) 60 nm; (middle) 82 nm; and (bottom) solar spectrum. Mean values and uncertainties (95% confidence interval) are respectively depicted by squares and error bars. In the middle graph, N-bearing species are enhanced by red squares. In the bottom graph, the discrimination between unsaturated and saturated species in each block is highlighted by red bars. (For interpretation of the references to colour in this figure, the reader is referred to the web version of this article.)

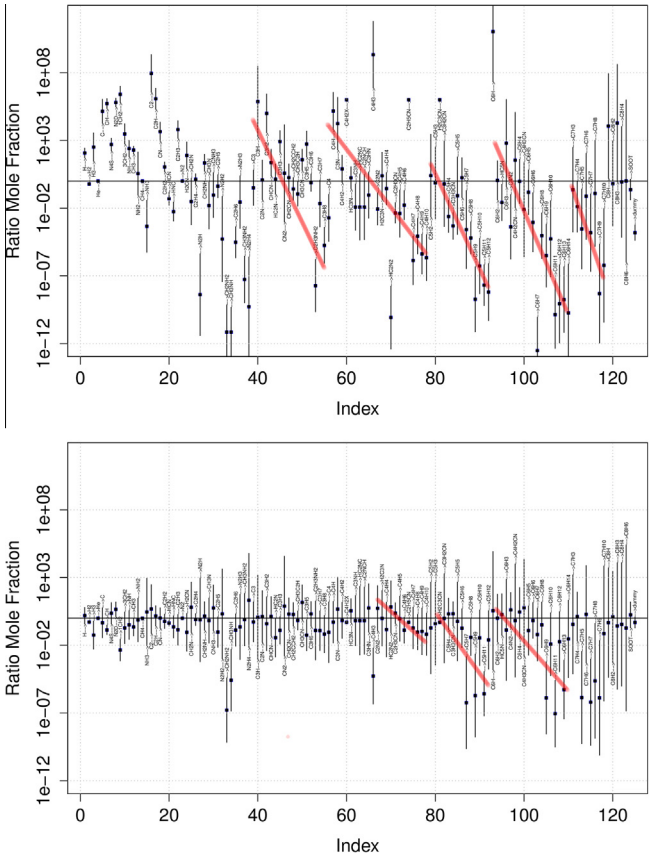

Fig. 13. Ratios of stationary concentrations in the case of low pressure (top) and low temperature (bottom) to those in the reference model. Mean values and uncertainties (95% confidence interval) are respectively denoted by squares and error bars. The discrimination between unsaturated and saturated species in each block is highlighted by red bars. (For interpretation of the references to color in this figure legend, the reader is referred to the web version of this article.)

of the branching ratios of the neutral channels of CH_4 photolysis (see Section 2.2.1, Fig. 1(b)). Far from the wavelengths where measurements exist, all neutral channel branching ratios are strongly uncertain (relative uncertainties ∼50–100%). Since CH_4 photolysis is a key process, this large uncertainty contributes significantly to the uncertainty budget of the species concentrations. Despite this substantial uncertainty increase, the previously identified promotion of the formation of N-bearing species by the exclusive production of N atoms by N_2 photolysis is significant for many species, such as $N(^4S), HCN, CH_2NH$, *etc.*

3.1.5.1.1. Pressure. In this simulation, the pressure P in the reactor is lowered from the reference case by a factor 10^6, which corresponds to the pressure around 850 km in Titan's upper atmosphere ($\sim 5 \times 10^{-4}$ Pa). To ensure that the averaged photoabsorption rates of N_2 and CH_4 are similar to the reference case, the reactor cell is elongated by the same factor to maintain the amount of gas ($L = 5 \times 10^5$ m).

Methane consumption is unaffected (Table 1), but the species distribution is strongly modified (Fig. 13 (top)). Some species (C_6H, C^+ and CN^+, for instance) are $\sim 10^8$ times more abundant than in the reference case, while others are reduced by similar amounts. We observe also a shift of the product distribution toward lower masses, signifying a limited growth.

A systematic discrimination between saturated and unsaturated species is notable in each Cx block. The mole fraction ratio of a species increases with its degree of unsaturation within a block (red lines in Fig. 13 (top)). In the C5 and C6 blocks, the ratio between the extremes can reach 10 orders of magnitude.

Assuming an unchanged composition of the reactive gas, lowering the pressure by a factor of 10^6 induces a lowering of the rate of all bimolecular reactions by a 10^{12} factor, while trimolecular reactions are slowed down by a factor of 10^{18}. The latter class contains the radical recombinations forming heavy saturated species. Trimolecular reactions are important at several mbar (see Section 3.1.3.2) and contribute significantly to the production of the most saturated species. However, this contribution vanishes rapidly as the pressure decreases, resulting in very low mole fractions of the most saturated species, *i.e.* C_5H_{11}, C_6H_{14}, *etc.*, and less lowered mole fractions of less saturated species, such as

C_5H_7 and C_6H_{10}. The most unsaturated species, *i.e.* $C_5H_3, C_6H_2 \ldots$ are not significantly affected.

3.1.5.2. Temperature. In this simulation, the temperature is lowered down to 150 K, close to that in Titan's ionosphere. The relative mole fractions are shown in Fig. 13 (bottom).

Compared to the reference simulation at 300 K, methane consumption is halved (Table 1), and few stationary concentrations are significantly altered, except those of heavy saturated neutral species. Lowering the temperature is not as effective to slow down the growth as lowering the pressure, because only neutral reaction rate constants decrease with temperature: there are only marginal temperature effects on photolysis cross-sections [70,71,43], or on ion–molecule reactions.

However, we observe a discrimination between the species of various degree of unsaturation in heavy species blocks (see Fig. 13 (bottom)). Among the main growth families, only the one driven by trimolecular reaction (G3) is notably slowed down by the decrease in temperature, provoking a depletion of heavy saturated species. Moreover, dissociative recombinations are slightly accelerated by the decreased temperature of thermalized electrons (between 35 and 70%), which contributes also to increase the production of unsaturated species.

3.2. Simulation of Imanaka & Smith's reactor

The model is now applied to Imanaka & Smith's reactor [27] with 60 nm irradiation, in the conditions of their experiment ($A = 1.2 \times 10^{-2}$ m^2, $L = 0.7$ m, $T = 300$ K, $P = 13$ Pa, $I_0 = 10^{16}$ ph s^{-1}, $N_2/CH_4 = 95/5$).

Methane consumption ($\rho_{CH_4} = 70\%$) is about three orders of magnitude above the reference case (Table 1), and the largest in our set of simulations. This is mostly due to a higher photon flux combined with a lower CH_4 partial pressure. The relative charge is about 4×10^{-7}. This charge is two orders of magnitude larger than for APSIS, because all photons at 60 nm contribute to ionization.

The experimental *in situ* MS and a simulated MS are compared in Fig. 14. The experimental spectrum is globally out of the 95% confidence interval of the simulated MS: the model systematically overestimates the production of unsaturated species and underestimates that of saturated species, by factors as large as 10^3.

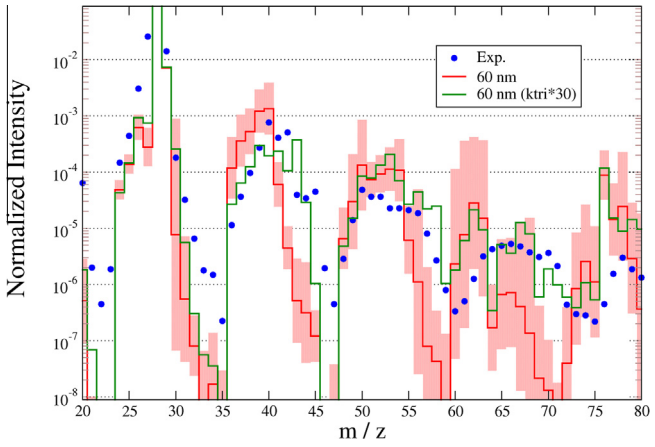

Fig. 14. Mass spectra for Imanaka and Smith [27] experiment at 60 nm: (solid lines) simulated neutral mass spectrum (red); same with trimolecular rate constants multiplied by a factor 30 (dark green) ; (blue dots) experimental *in situ* gas phase MS. The MS intensities are normalized with respect to that of N_2. The 95% confidence intervals of simulated spectra for the first case is marked by a shaded area. (For interpretation of the references to colour in this figure caption, the reader is referred to the web version of this article.)

A series of factors might be responsible for this discrepancy:

- The mass spectrometer in Imanaka & Smith's experiments was used at too high pressure to retain the linearity of its MS signals, as discussed for the APSIS experiments in Peng et al. [28]. However, the non-linearity of MS signals appears in a relatively uniform way in a band, therefore this argument cannot explain the systematic differential effects observed in all bands.
- The stable species considered in the simulated spectrum only accounts for a minor part ($\sim 10\%$) of total mass of products in the case of Imanaka & Smith's reactor. The radicals, accounting for a large part of the total mass ignored in the simulated spectrum, are certainly an important source of disagreement. However, the factor 1000 between the saturated parts of measured and simulated MS bands is still not explained. Assuming that the chemical model is basically correct, the saturated part could have a concentration (not an intensity in the simulated MS) comparable to the unsaturated part in the same block, only if large radicals ignored in the simulated MS are (nearly) saturated, which cannot be the case. Even in the homogeneous model of the APSIS experiments, at a higher pressure disfavoring the growth of unsaturated species, these are still dominant in the blocks of heavy species. Therefore, the assumption of a correct chemistry is not true, *i.e.* the present homogeneous model is not adequate to simulate the chemistry occurring during Imanaka & Smith's experiments.

Following the same logic as for the APSIS reactor, we address the limitations of homogeneous chemistry, by enhancing the trimolecular rate constants. In view of lower pressure and larger internal surface-to-volume ratio of Imanaka & Smith's reactor than the APSIS reactor, both resulting in a larger relative contribution of heterogeneous chemistry, we tested three cases with 10, 30 and 100 times faster trimolecular rate constants. As for the reference case, the unsaturated part of MS bands is slightly lowered and the saturated part is significantly increased by this modification. As trimolecular rate constants are amplified, the unsaturated part of the C3–C5 bands of the simulated MS gradually approaches the experimental results and their saturated part reaches and then overtakes the measured values.

The simulated spectrum corresponding to a factor 30 is shown in Fig. 14. Though still not satisfactory, for instance in the saturated

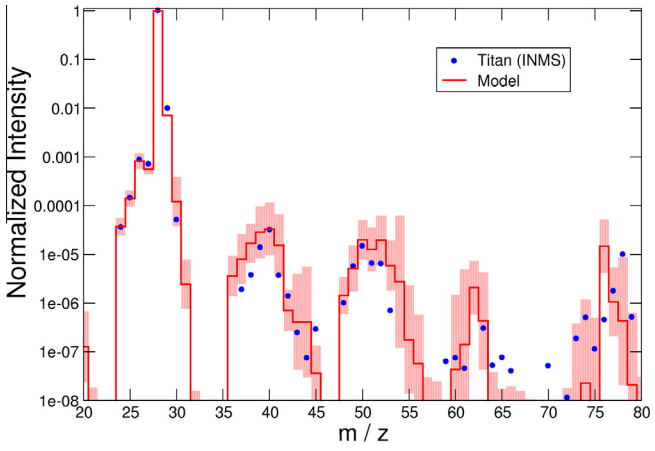

Fig. 15. Simulated neutral mass spectrum in Titan-like conditions (solid lines, red) compared to INMS neutral MS [9] (blue points). The MS intensities are normalized with respect to that of N_2. The 95% confidence intervals of simulated spectra are shown by shaded area. (For interpretation of the references to colour in this figure caption, the reader is referred to the web version of this article.)

part of the C4–C6 band which is still overestimated, the agreement between the simulated spectrum and the experimental one is notably improved, especially for the saturated part. This may illustrate the very important effect of heterogeneous chemistry in this reactor, probably even stronger than in APSIS, because of the more favorable (tubular) geometry and lower pressure.

As discussed by Imanaka and Smith [27], the overestimation in Titan's atmospheric models of the density of C_4N_2 (m/z 62 and 76) is due to a lack of loss processes for CHCN. This is verified here also for experimental laboratory conditions. In the present case, the overestimation is by more than two orders of magnitude (Fig. 14). This discrepancy is possibly higher than the ones noted for Titan modeling [27], see also Fig. 15. This would suggest that wall effects might be an efficient sink for CHCN in Imanaka & Smith setup. In any case, there is an urgent need of data on the reactivity of CHCN, either in homogeneous or heterogeneous conditions.

3.3. Simulation of a reactor in Titan's ionospheric conditions

Combining the solar spectrum irradiation, low T and low P cases studied above, one obtains a set of conditions reminiscent of Titan's ionosphere. Without aiming at a realistic simulation of this environment, a few adaptations of the parameters are necessary to get more representative conditions, such as adapting the photon flux and removing the carrier gas. The main difference of physical conditions between Titan atmosphere and the present 1-cell model is the effective gas residence time corresponding to complex transport processes at Titan [72–74], which was adjusted: an effective residence time of $\tau_r = 2.8 \times 10^6$ s was found to give a globally satisfying products distribution (Fig. 15). It is 10^4 times that in the reference case and about 10 times larger than the transport time constant at 850 km in Titan's atmosphere [72].

Methane consumption is 2.2%, about 30 times that of APSIS simulation, a consequence of the much increased residence time, and the ionization ratio is about 10^{-8}. This value is in good agreement with an estimation of the ionization ratio in Titan's ionosphere – the electron number density (about 10^2 cm^{-3}) over N_2 number density (10^{10}–10^{11} cm^{-3}) – at 950 km [75], which corresponds to the altitude for the INMS spectrum used for comparison below.

Table 4
Consensus list of key reactions identified for the "Titan's ionosphere" simulation, their rate constant uncertainty factor F_k in the conditions of the simulation, the corresponding number $N_>$ of species used for selection, and their S score (see text). Bold characters indicate the maximum in each column.

Reaction	F_k	Scores	
		$N_>$	S
$^1CH_2 + N_2 \longrightarrow {}^3CH_2 + N_2$	2.0	**41**	**7.0**
$^1CH_2 + CH_4 \longrightarrow 2CH_3$	1.5	36	6.3
$C_2H_4 + h\nu \longrightarrow C_2H_3 + H$	1.3	35	3.6
$C_2H_4 + h\nu \longrightarrow C_2H_4^+ + e^-$	1.2	26	3.5
$C_2H_4 + h\nu \longrightarrow C_2H_2 + H_2$	1.4	25	3.3
$N(^2D) + C_2H_4 \longrightarrow CH_3CN + H$	1.5	34	6.2
$H + CH \longrightarrow C + H_2$ [a]	**7.4**	27	5.7
$N_2 + h\nu \longrightarrow N(^4S) + N(^2D)$ [b,a]	< 1.1	23	4.6
$N_2 + h\nu \longrightarrow N_2^+ + e^-$ [b]	< 1.1	20	4.5
$C_2H_2 + h\nu \longrightarrow C_2H + H$	1.5	21	3.6
$C_2H + C_2H_2 \longrightarrow C_4H_2 + H$	2.1	18	4.3
$N(^2D) + C_2H_2 \longrightarrow CHCN + H$	1.3	18	3.3
$CH_4 + h\nu \longrightarrow CH_4^+ + e^-$	1.2	17	4.2
$CH_4 + h\nu \longrightarrow CH_3^+ + H + e^-$	1.3	16	3.0
$CH_4 + h\nu \longrightarrow CH^+ + H_2 + H + e^-$ [b]	1.4	17	3.8

[a] key reactions in common with Hébrard et al. [32].
[b] key reactions shared with the APSIS list (Table 2).

In Fig. 15, the simulated MS is compared to the INMS neutral spectrum of T19 flyby between 950 and 1000 km, published in Waite et al. [9]. The agreement between the observations and the simulated spectrum for Titan is remarkably better than for either the APSIS (Fig. 5) or Imanaka & Smith's (Fig. 14) experiments. In particular, one notes a good reproduction of the preponderance of unsaturated species within each block. This confirms the effect of low pressure and temperature underlined above (Sections 3.1.5.1.1 and 3.1.5.2) to favor the growth of unsaturated species.

The preponderance of unsaturated species at Titan indirectly supports our hypothesis that the reactor's metallic wall plays an important role in the production of saturated species in the laboratory simulation experiments, simply because in Titan's atmosphere, there is no such an efficient "wall" that promotes heterogeneous chemistry. Note however that wall effects on the INMS antechamber have been discussed by Vuitton et al. [11], and that heterogeneous reactions promoted by the aerosols are beginning to be studied [76].

The reproduction of the fact that C6 block's concentration is larger than C5 block's also validates the present reaction scheme in general terms. Though underestimated by the model, C_6H_6 (mainly at m/z 78) stands out as a major heavy product. Being highly unsaturated, it is efficiently formed in Titan's atmosphere thanks to the physical conditions for its growth, *i.e.* low pressure and low temperature. On the other hand, overestimation of the intensities at m/z 62 and m/z 76, associated with C_4N_2, is due to a lack of loss pathways for CHCN, as discussed in Section 3.2.

3.3.1. Key reactions

For comparison with the key reactions identified in a neutral model of Titan's chemistry by Hébrard et al. [32], we used the same procedure as in Section 3.1.3 on the present results. The list of key reactions is reported in Table 4. The intersection with Hébrard et al. [32] is reduced to two reactions $N_2 + h\nu \longrightarrow N(^4S) + N(^2D)$ and $H + CH \longrightarrow C + H_2$. The first one has already been evoked in Section 3.1.3. The second reaction has a very large uncertainty factor and has been shown to be able to induce different chemical regimes in Dobrijevic et al. [77]. A better estimation of this rate constant remains thus a priority for Titan's chemistry modeling.

4. Conclusion

APSIS experiments have been studied by a 1-cell model with a fully coupled chemical scheme, *i.e.* involving all photolysis, bimolecular, trimolecular, ion–molecule reactions and dissociative recombinations with available kinetic data. The methane consumption is found acceptable and the production in Cx blocks is in good agreement with the experimental MS measurements.

Ion chemistry and the full dissociative recombination scheme have been shown to be important in the model. Without them, the production of heavy species and heavy unsaturated species, respectively, are drastically lowered. By sensitivity analysis, photolysis and several reactions sensitive to pressure, mostly trimolecular reactions, appear as global *key reactions*. Influential photolysis reactions are consistent with the previous studies [32,39], and influential trimolecular reactions result from the relatively high pressure in the APSIS reactor.

Block patterns are observed in a species correlation matrix, indicating the importance of the addition of small units for molecular growth. Cluster analysis of the species correlation matrix reveals three major clusters of species: G1, where the growth of unsaturated species has been shown to be promoted by C_2H_2 through ion–molecule reactions; G2, in which the nitrogen

incorporation in hydrocarbons plays a central role; and G3, where the formation of heavy saturated species is ensured by trimolecular termination of radicals. The global efficiency of the G1 family among the three is clearly identified, *i.e.* the growth pathways of *unsaturated* species via *ion* chemistry are the most efficient to form heavy species.

This completes the discussion of Plessis et al. [25] about the species responsible for the promotion of the chemistry with a full dissociative recombination scheme. Plessis et al. [25] pointed out two antagonistic effects of dissociative recombination: a global chemical lysis of heavy ions and a promotion of the molecular growth due to the production of numerous small reactive species. In fact, the non H-loss dissociative recombination channels, through which many of small neutrals including C1 and C2 are produced, supply the main unsaturated reactants of the G1 cluster, but not saturated ones. In the APSIS model, these non H-loss channels increase the production rate of C_2H_2 by a factor of ~10, leading to a more efficient growth of unsaturated species. Therefore dissociative recombination produces small unsaturated species, especially C_2H_2, enhancing the most efficient growth pathways. This illustrates the promoting effects of dissociative recombination discussed by Plessis et al. [25], and makes them able to overtake the chemical lysis effect.

Titan's ionosphere meets simultaneously the conditions favoring the growth of unsaturated species, *i.e.* low pressure and low temperature, leading to densities of unsaturated species, detected in an INMS neutral spectrum, in agreement with our modeling results. In contrast, the simulated MS for the APSIS and Imanaka & Smith's experiments are not in good agreement with the experimental data in the saturated part of each Cx block. The model systematically underestimates the intensities of the saturated parts, revealing the insufficiency of homogeneous chemistry, which favors the growth of unsaturated species. If the recombinations catalyzed by the reactor's walls are accounted for, the simulated MS are significantly improved, which strongly suggests the existence of noticeable wall effects in the laboratory simulation setups.

Based on this analysis, we have well identified competing homogeneous and heterogeneous chemistries in the reactors. The former essentially involves the growth of unsaturated species and is representative of the chemistry in Titan's upper atmosphere, and the latter promotes the production of saturated species and can be regarded as a bias of laboratory reactors. It was also shown that the unsaturated parts in the simulated MS are much less sensitive than the saturated parts to our *ad hoc* implementation of heterogeneous chemistry. Therefore one may consider preferentially the experimental results on unsaturated species for a qualitative laboratory simulation of Titan's photochemistry.

The existence of wall effects also reveals the needs for further studies: simulation experiments at relatively low temperature (*e.g.* at ~0 °C, leading to wall recombinations ~100–1000 times slower than at room temperature [56]) or using less catalytic wall materials to reduce these effects [78], and measurements of the kinetic parameters of involved heterogeneous reactions for their appropriate consideration in the model.

Several elementary processes have been identified at different stages of the present study as needing new or improved kinetic data, often confirming the data requests of other authors: the dissociative recombination rate and branching ratios for $CH_2NH_2^+$ [17]; the rate constant of the CH + H reactions [32,77]; new reactions consuming CHCN [27]; the photolysis branching ratios of CH_4 around 80 nm, and more generally over the whole 80–140 nm range. These parameters are important sources of uncertainty and/or bias in the model predictions, and they are urgently needed to improve the detailed chemical modeling of N_2/CH_4 plasmas and Titan's ionosphere.

References

[1] Wilson EH, Atreya SK. Chemical sources of haze formation in Titan's atmosphere. Planet Space Sci 2003;51:1017–33. http://dx.doi.org/10.1016/j.pss.2003.06.003.

[2] Wilson EH, Atreya SK. Current state of modeling the photochemistry of Titan's mutually dependent atmosphere and ionosphere. J Geophys Res 2004;109:E06002. http://dx.doi.org/10.1029/2003JE002181.

[3] Cravens TE, Robertson IP, Clark J, Wahlund JE, Waite JH, Ledvina SA, Niemann HB, Yelle RV, Kasprzak WT, Luhmann JG, McNutt RL, Ip WH, De La Haye V, Müller-Wodarg I, Young DT, Coates AJ. Titan's ionosphere: model comparisons with Cassini Ta data. Geophys Res Lett 2005;32:L12108. http://dx.doi.org/10.1029/2005GL023249.

[4] Atreya SK, Adams EY, Niemann HB, Demick-Montelara JE, Owen TC, Fulchignoni M, Ferri F, Wilson EH. Titan's methane cycle. Planet Space Sci 2006;54:1177–87. http://dx.doi.org/10.1016/j.pss.2006.05.028.

[5] Cravens T, Robertson I, Waite Jr J, Kasprzak W, Keller C, Ledvina S, Niemann H, Luhmann J, McNutt R, Ip W, Haye VDL, Mueller-Wodarg I, Wahlung J, Anicich V, Vuitton V. Composition of Titan's ionosphere. Geophys Res Lett 2006;33:L07312. http://dx.doi.org/10.1029/2005GL025575.

[6] Vuitton V, Yelle R, Anicich V. The nitrogen chemistry of Titan's upper atmosphere revealed. Astrophys J 2006;647:L175–8. http://dx.doi.org/10.1086/507467.

[7] Atreya SK. Titan's organic factory. Science 2007;316:843–5. http://dx.doi.org/10.1126/science.1141869.

[8] Vuitton V, Yelle R, McEwan M. Ion chemistry and N-containing molecules in Titan's upper atmosphere. Icarus 2007;191:722–42. http://dx.doi.org/10.1016/j.icarus.2007.06.023.

[9] Waite J, Young D, Cravens T, Coates A, Crary F, Magee B, Westlake J. The process of tholin formation in Titan's upper atmosphere. Science 2007;316:870–5. http://dx.doi.org/10.1126/science.1139727.

[10] De La Haye V, Waite J, Cravens T, Robertson I, Lebonnois S. Coupled ion and neutral rotating model of Titan's upper atmosphere. Icarus 2008;197:110–36. http://dx.doi.org/10.1016/j.icarus.2008.03.022.

[11] Vuitton V, Yelle RV, Cui J. Formation and distribution of benzene on Titan. J Geophys Res 2008;113:E05007. http://dx.doi.org/10.1029/2007JE002997.

[12] Crary FJ, Magee BA, Mandt K, Waite Jr JH, Westlake J, Young DT. Heavy ions, temperatures and winds in Titan's ionosphere: combined Cassini CAPS and INMS observations. Planet Space Sci 2009;57(14–15):1847–56. http://dx.doi.org/10.1016/j.pss.2009.09.006.

[13] Krasnopolsky V. A photochemical model of Titan's atmosphere and ionosphere. Icarus 2009;201:226–56. http://dx.doi.org/10.1016/j.icarus.2008.12.038.

[14] Vuitton V, Lavvas P, Yelle R, Galand M, Wellbrock A, Lewis G, Coates A, Wahlund J-E. Negative ion chemistry in Titan's upper atmosphere. Planet Space Sci 2009;57:1558–72. http://dx.doi.org/10.1016/j.pss.2009.04.004.

[15] Vuitton V, Yelle R, Lavvas P. Composition and chemistry of Titan's thermosphere and ionosphere. Philos Trans R Soc A Math Phys Eng Sci 2009;367:729–41. http://dx.doi.org/10.1098/rsta.2008.0233.

[16] Wilson EH, Atreya SK. Titan's carbon budget and the case of the missing ethane. J Phys Chem A 2009;113(42):11221–6. http://dx.doi.org/10.1021/jp905535a.

[17] Yelle RV, Vuitton V, Lavvas P, Klippenstein SJ, Smith MA, Hörst SM, Cui J. Formation of NH_3 and CH_2NH in Titan's upper atmosphere. Faraday Discuss 2010;147:31–49. http://dx.doi.org/10.1039/c004787m.

[18] Westlake JH, Waite Jr JH, Mandt KE, Carrasco N, Bell JM, Magee BA, Wahlund J-E. Titan's ionospheric composition and structure: photochemical modeling of Cassini INMS data. J Geophys Res 2012;117:E01003. http://dx.doi.org/10.1029/2011JE003883.

[19] Lavvas P, Coustenis A, Vardavas I. Coupling photochemistry with haze formation in Titan's atmosphere, Part I: model description. Planet Space Sci 2008;56:27–66. http://dx.doi.org/10.1016/j.pss.2007.05.026.

[20] Lavvas P, Coustenis A, Vardavas I. Coupling photochemistry with haze formation in Titan's atmosphere, Part II: results and validation with Cassini/Huygens data. Planet Space Sci 2008;56:67–99. http://dx.doi.org/10.1016/j.pss.2007.05.027.

[21] Wahlund J-E, Galand M, Müller-Wodarg I, Cui J, Yelle R, Crary F, Mandt K, Magee B, Waite Jr J, Young D, Coates A, Garnier P, Ågren K, André M, Eriksson A, Cravens T, Vuitton V, Gurnett D, Kurth W. On the amount of heavy molecular ions in Titan's ionosphere. Planet Space Sci 2009;57:1857–65. http://dx.doi.org/10.1016/j.pss.2009.07.014.

[22] Lavvas P, Yelle RV, Koskinen T, Bazin A, Vuitton V, Vigren E, Galand M, Wellbrock A, Coates AJ, Wahlund J-E, Crary FJ, Snowden D. Aerosol growth in Titan's ionosphere. Proc Natl Acad Sci 2013;110(8):2729–34. http://dx.doi.org/10.1073/pnas.1217059110.

[23] Plessis S, Carrasco N, Pernot P. Knowledge-based probabilistic representations of branching ratios in chemical networks: the case of dissociative recombinations. J Chem Phys 2010;133:134110. http://dx.doi.org/10.1063/1.3479907.

[24] Pernot P, Plessis S, Carrasco N. Probabilistic representations of partial branching ratios: bridging the gap between experiments and chemical models. J Phys Conf Ser 2011;300:012027. http://dx.doi.org/10.1088/1742-6596/300/1/012027.

[25] Plessis S, Carrasco N, Dobrijevic M, Pernot P. Production of neutral species in Titan's ionosphere through dissociative recombination of ions. Icarus 2012;219:254–66. http://dx.doi.org/10.1016/j.icarus.2012.02.032.

[26] Thissen R, Vuitton V, Lavvas P, Lemaire J, Dehon C, Dutuit O, Smith MA, Turchini S, Catone D, Yelle RV, Pernot P, Somogyi A, Coreno M. Laboratory studies of molecular growth in the titan ionosphere. J Phys Chem A 2009;113:11211–20. http://dx.doi.org/10.1021/jp9050353.
[27] Imanaka H, Smith MA. Formation of nitrogenated organic aerosols in the Titan upper atmosphere. Proc Natl Acad Sci 2010;107:12423–8. http://dx.doi.org/10.1073/pnas.0913353107.
[28] Peng Z, Gautier T, Carrasco N, Pernot P, Giuliani A, Mahjoub A, Correia J-J, Buch A, Bénilan Y, Szopa C, Cernogora G. Titan's atmosphere simulation experiment using continuum UV-VUV synchrotron radiation. J Geophys Res Planets 2013;118:778–88. http://dx.doi.org/10.1002/jgre.20064.
[29] Giuliani A, Jamme F, Rouam V, Wien F, Giorgetta J-L, Lagarde B, Chubar O, Bac S, Yao I, Rey S, Herbeaux C, Marlats J-L, Zerbib D, Polack F, Refregiers M. DISCO: a low-energy multipurpose beamline at synchrotron SOLEIL. J Synchrotron Radiat 2009;16:835–41. http://dx.doi.org/10.1107/S0909049509034049.
[30] Giuliani A, Yao I, Lagarde B, Rey S, Duval J-P, Rommeluere P, Jamme F, Rouam V, Wein F, De Oliveira C, Ros M, Lestrade A, Desjardins K, Giorgetta J-L, Laprevote O, Herbaux C, Refregiers M. A differential pumping system to deliver windowless VUV photons at atmospheric pressure. J Synchrotron Radiat 2011;18:546–9. http://dx.doi.org/10.1107/S0909049511016517.
[31] Hébrard E, Dobrijevic M, Bénilan Y, Raulin F. Photochemical kinetics uncertainties in modeling Titan's atmosphere: a review. J Photochem Photobiol A: Chem 2006;7:211–30. http://dx.doi.org/10.1016/j.jphotochemrev.2006.12.004.
[32] Hébrard E, Dobrijevic M, Pernot P, Carrasco N, Bergeat A, Hickson KM, Canosa A, Le Picard SD, Sims IR. How measurements of rate coefficients at low temperature increase the predictivity of photochemical models of Titan's atmosphere. J Phys Chem A 2009;113:11227–37. http://dx.doi.org/10.1021/jp905524e.
[33] Gans B, Peng Z, Carrasco N, Gauyacq D, Lebonnois S, Pernot P. Impact of a new wavelength-dependent representation of methane photolysis branching ratios on the modeling of Titan's atmospheric photochemistry. Icarus 2013;223:330–43. http://dx.doi.org/10.1016/j.icarus.2012.11.024.
[34] Carrasco N, Alcaraz C, Dutuit O, Plessis S, Thissen R, Vuitton V, Yelle R, Pernot P. Sensitvity of a Titan ionospheric model to the ion–molecule reaction parameters. Planet Space Sci 2008;55:1644–57. http://dx.doi.org/10.1016/j.pss.2008.04.007.
[35] Dutuit O, Carrasco N, Thissen R, Vuitton V, Alcaraz C, Pernot P, Balucani N, Casavecchia P, Canosa A, Picard SL, Loison J-C, Herman Z, Zabka J, Ascenzi D, Tosi P, Franceschi P, Price SD, Lavvas P. Critical Review of N, N+, N+ 2, N++, and N++ 2 Main Production Processes and Reactions of Relevance to Titan's Atmosphere. Astrophys J Suppl Ser 2013;204:20. http://dx.doi.org/10.1088/0067-0049/204/2/20.
[36] Eland JH. Double photoionisation spectra of methane, ammonia and water. Chem Phys 2006;323:391–6. Available from: <http://dx.doi.org/10.1016/j.chemphys.2005.09.047>.
[37] De Bleecker K, Bogaerts A, Goedheer W. Detailed modeling of hydrocarbon nanoparticle nucleation in acetylene discharges. Phys Rev E 2006;73:026405. http://dx.doi.org/10.1103/PhysRevE.73.026405.
[38] Hébrard E, Dobrijevic M, Bénilan Y, Raulin F. Photochemical kinetics uncertainties in modeling Titan's atmosphere: first consequences. Planet Space Sci 2007;55:1470–89. http://dx.doi.org/10.1016/j.pss.2007.04.006.
[39] Peng Z, Dobrijevic M, Hebrard E, Carrasco N, Pernot P. Photochemical modeling of Titan atmosphere at the 10 percent uncertainty horizon. Faraday Discuss 2010;147:137–53. http://dx.doi.org/10.1039/c003366a.
[40] Peng Z, Cailliez F, Dobrijevic M, Pernot P. Null Variance Altitudes for the photolysis rate constants of species with barometric distribution: illustration on Titan upper atmosphere modeling. Icarus 2012;218:950–5. http://dx.doi.org/10.1016/j.icarus.2012.02.006.
[41] Carrasco N, Pernot P. Modeling of branching ratio uncertainty in chemical networks by Dirichlet distributions. J Phys Chem A 2007;111:3507–12. http://dx.doi.org/10.1021/jp067306v.
[42] Carrasco N, Dutuit O, Thissen R, Banaszkiewicz M, Pernot P. Uncertainty analysis of bimolecular reactions in Titan ionosphere chemistry model. Planet Space Sci 2007;55:141.
[43] Chen F, Wu C. Temperature-dependent photoabsorption cross sections in the VUV-UV region. I. Methane and ethane. J Quant Spectrosc Radiat Transfer 2004;85(2):195–209. http://dx.doi.org/10.1016/S0022-4073(03)00225-5.
[44] Huebner W, Link W. Photo cross-sections and rate coefficients; 2011. <http://amop.space.swri.edu/>.
[45] Anicich V. Evaluated bimolecular ion–molecule gas phase kinetics of positive ions for use in modelling planetary atmospheres, cometary comae and interstellar clouds. J Phys Chem Ref Data 1993;22:1469–569. http://dx.doi.org/10.1063/1.555940.
[46] Press WH, Teukolsky SA, Vetterling WT, Flannery BP. Numerical recipes. Cambridge University Press; 1992.
[47] Shampine LF, Sommeijer BP, Verwer JG. IRKC: an IMEX solver for stiff diffusion–reaction PDEs. J Comput Appl Math 2006;196:485–97. http://dx.doi.org/10.1016/j.cam.2005.09.014.
[48] Verwer J, Sommeijer B. An implicit-explicit Runge–Kutta–Chebyshev scheme for diffusion–reaction equations. SIAM J Sci Comput 2004;25(5):1824–35. http://dx.doi.org/10.1137/S1064827503429168.
[49] BIPM, IEC, IFCC, ILAC, ISO, IUPAC, IUPAPOIML. Evaluation of measurement data – supplement 1 to the Guide to the expression of uncertainty in measurement – Propagation of distributions using a Monte Carlo method. Technical Report 101:2008, Joint Committee for Guides in Metrology, JCGM; 2008.
[50] Puccio MA, Miller JH. Detection of trace hydrocarbons in flames using direct sampling mass spectrometry coupled with multilinear regression analysis. Anal Chem 2010;82:5160–8. http://dx.doi.org/10.1021/ac1003823.
[51] Stein S. NIST chemistry webbook. NIST standard reference database number 69, chapter Mass Spectra. National Institute of Standards and Technology, Gaithersburg MD, 20899; 2013. (Retrieved August 30, 2013).
[52] Carrasco N, Gautier T, Essebbar E, Pernot P, Cernogora G. Volatile products controlling Titan's tholins production. Icarus 2012;219:230–40. http://dx.doi.org/10.1016/j.icarus.2012.02.034.
[53] Dobrijevic M, Dutour I. The distribution of hydrocarbons in Titan's atmosphere: an evolutionary algorithm-based model. Planet Space Sci 2007;55(14):2128–36. http://dx.doi.org/10.1016/j.pss.2007.06.003.
[54] Carrasco E, Jimenez-Redondo M, Tanarro I, Herrero VJ. Neutral and ion chemistry in low pressure dc plasmas of H2/N2 mixtures: routes for the efficient production of NH3 and NH4+. Phys Chem Chem Phys 2011;13:19561–72. http://dx.doi.org/10.1039/C1CP22284H.
[55] Jacq S, Cardinaud C, Brizoual LL, Granier A. H atom surface loss kinetics in pulsed inductively coupled plasmas. Plasma Sources Sci Technol 2013;22(5):055004. http://dx.doi.org/10.1088/0963-0252/22/5/055004.
[56] Gorodetsky A, Zalavutdinov R, Zakharov A, Vnukov S, Varshavskaya I, Makhankov A, Mazul I, Federici G. Increased recombination of CH_3 radicals on stainless steel. J Nucl Mater 2005:892–6. http://dx.doi.org/10.1016/j.jnucmat.2004.10.133.
[57] Wakelam V, Smith IWM, Herbst E, Troe J, Geppert W, Linnartz H, Öberg K, Roueff E, Agundez M, Pernot P, Cuppen HM, Loison J-C, Talbi D. Reaction networks for interstellar chemical modelling: improvements and challenges. Space Sci Rev 2010;156:13–72. http://dx.doi.org/10.1007/s11214-010-9712-5.
[58] Dobrijevic M, Hébrard E, Plessis S, Carrasco N, Bruno-Claeys M, Pernot P. Comparison of methods for the determination of key reactions in chemical systems: Application to Titan's atmosphere. Adv Space Res 2010;45:77–91. http://dx.doi.org/10.1016/j.asr.2009.06.005.
[59] Rosi M, Falcinelli S, Balucani N, Casavecchia P, Skouteris D. A theoretical study of formation routes and dimerization of methanimine and implications for the aerosols formation in the upper atmosphere of Titan. In: Murgante B, Misra S, Carlini M, Torre CM, Nguyen H-Q, Taniar D, Apduhan BO, Gervasi O, editors. Computational science and its applications – ICCSA 2013. Lecture notes in computer science, vol. 7971. Berlin Heidelberg: Springer; 2013. p. 47–56. http://dx.doi.org/10.1007/978-3-642-39637-3_4.
[60] R Development Core Team. R: A language and environment for statistical computing. R foundation for statistical computing, Vienna, Austria; 2012. <http://www.R-project.org>.
[61] Murtagh F, Contreras P. Algorithms for hierarchical clustering: an overview. Wiley Interdiscip Rev Data Min Knowl Discovery 2012;2:86–97. http://dx.doi.org/10.1002/widm.53.
[62] van Krevelen W. Graphical-statistical method for the study of structure and reaction processes of coal. Fuel 1950;29:269–84.
[63] Wu Z, Rodgers R, Marshall A. Two- and three-dimensional van Krevelen diagrams: A graphical analysis complementary to the kendrick mass plot for sorting elemental compositions of complex organic mixtures based on ultrahigh-resolution broadband Fourier Transform Ion Cyclotron Resonance mass measurements. Anal Chem 2004;76(9):2511–6. http://dx.doi.org/10.1021/ac0355449.
[64] Benedikt J. Plasma-chemical reactions: low pressure acetylene plasmas. J Phys D: Appl Phys 2010;43(4):043001. http://dx.doi.org/10.1088/0022-3727/43/4/043001.
[65] Kaiser RI, Mebel AM. On the formation of polyacetylenes and cyanopolyacetylenes in Titan's atmosphere and their role in astrobiology. Chem Soc Rev 2012;41:5490–501. http://dx.doi.org/10.1039/C2CS35068H.
[66] Balucani N. Elementary reactions of N atoms with hydrocarbons: first steps towards the formation of prebiotic N-containing molecules in planetary atmospheres. Chem Soc Rev 2012;41:5473–83. http://dx.doi.org/10.1039/C2CS35113G.
[67] Floyd LE, Reiser PA, Crane PC, Herring LC, Prinz DK, Brueckner GE. Solar cycle 22 UV spectral irradiance variability: current measurements by SUSIM UARS. Sol Phys 1998;177:79–87. http://dx.doi.org/10.1023/A:1004907902440.
[68] BIPM, IEC, IFCC, ILAC, ISO, IUPAC, IUPAP, OIML. Evaluation of measurement data – guide to the expression of uncertainty in measurement (GUM). Technical Report 100:2008, Joint Committee for Guides in Metrology, JCGM; 2008.
[69] Imanaka H, Smith M. Role of photoionization in the formation of complex organic molecules in Titan's upper atmosphere. Geophys Res Lett 2007;34:L02204. http://dx.doi.org/10.1029/2006GL028317.
[70] Wu CYR, Chen FZ, Judge DL. Temperature-dependent photoabsorption cross sections in the VUV-UV region: Ethylene. J Geophys Res Planets 2004;109(E7):E07S15. http://dx.doi.org/10.1029/2003JE002180.
[71] Jolly A, Benilan Y. Review of quantitative spectroscopy of polyynes. J Quant Spectrosc Radiat Transfer 2008;109(6):963–73. http://dx.doi.org/10.1016/j.jqsrt.2007.12.010.

[72] De La Haye, V. Corona formation and heating efficiencies in titan's upper atmosphere: construction of a coupled ion, neutral and thermal structure model to interpret the first inms cassini data [PhD thesis]. The University of Michigan; 2005.
[73] Yelle RV, Cui J, Mueller-Wodarg ICF. Methane escape from Titan's atmosphere. J Geophys Res Planets 2008;113:E10003. http://dx.doi.org/10.1029/2007JE003031.
[74] Strobel DF. Titan's hydrodynamically escaping atmosphere: escape rates and the structure of the exobase region. Icarus 2009;202:632–41. http://dx.doi.org/10.1016/j.icarus.2009.03.007.
[75] Mandt KE, Gell DA, Perry M, Hunter Waite J, Crary FA, Young D, Magee BA, Westlake JH, Cravens T, Kasprzak W, Miller G, Wahlund J-E, Agren K, Edberg NJT, Heays AN, Lewis BR, Gibson ST, de la Haye V, Liang M-C. Ion densities and composition of Titan's upper atmosphere derived from the Cassini ion neutral mass spectrometer: analysis methods and comparison of measured ion densities to photochemical model simulations. J Geophys Res Planets 2012;117:2156–202. http://dx.doi.org/10.1029/2012JE004139.
[76] Sekine Y, Lebonnois S, Imanaka H, Matsui T, Bakes EL, McKay CP, Khare BN, Sugita S. The role of organic haze in Titan's atmospheric chemistry: II. Effect of heterogeneous reaction to the hydrogen budget and chemical composition of the atmosphere. Icarus 2008;194:201–11. http://dx.doi.org/10.1016/j.icarus.2007.08.030.
[77] Dobrijevic M, Carrasco N, Hébrard E, Pernot P. Epistemic bimodality and kinetic hypersensitivity in photochemical models of Titan's atmosphere. Planet Space Sci 2008;56:1630–43. http://dx.doi.org/10.1016/j.pss.2008.05.016.
[78] Oinuma G, Inanaga Y, Tanimura Y, Kuzumoto M, Tabata Y, Watanabe K. A comparative study of the surface recombination of nitrogen atoms on various materials at atmospheric pressure. J Phys D Appl Phys 2010;43:255202. http://dx.doi.org/10.1088/0022-3727/43/25/255202.